Please cite the following article as:

Zamani, N., Marban, D. L., Sandve, T. H., & Gasda, S. E. (2026). Unraveling salt precipitation mechanisms in geological CO_2 storage: insights into dominant driving forces. *InterPore Journal*. Advance online publication. https://doi.org/10.69631/zhna7r09

Received: 12 Aug- 2025
Accepted: 24 Feb. 2026
Published Online (accepted version): 18 Mar. 2026

Unraveling salt precipitation mechanisms in geological CO_2 storage: insights into dominant driving forces

Nematollah Zamani[1], David Landa-Marbán[1], Tor Harald Sandve[1], Sarah E. Gasda[1,2]*

[1] Department of Energy and Technology, NORCE Norwegian Research Centre AS, Nygårdstangen, 5838, Bergen, Norway

[2] Department of Physics and Technology, University of Bergen, Allégaten 55, 5007, Bergen, Norway

* Corresponding author:

E-mail: Nematollah.zamani@norceresearch.no

Abstract

Salt precipitation during geological CO_2 storage (GCS) in saline aquifers can impair the injectivity of large-scale projects. Laboratory studies indicate that this process is sensitive to capillary force, but scaling-up to field conditions is complex due to radial flow, gravity, and geological heterogeneity. This study utilizes 3D simulations to characterize salt precipitation mechanisms in realistic storage formations. Non-dimensional groups, e.g., capillary number (Ca) and gravity number (Gr), are used to characterize the relative impact of capillary, viscous, and gravity forces on salt formation. Three distinct regimes emerge for homogeneous systems: (1) capillary-dominated regime for $Ca < 1$ with severe salt precipitation at the inlet; (2) viscous-dominated regime for $Ca > 1$ and $Gr < 0.2$ with low-to-moderate salt precipitation; and (3) gravity-dominated regime for $Ca > 1$ and $Gr > 0.2$ where gravity override leads to localization of salt deposits inside the reservoir. The Ca-Gr regimes generally hold for heterogeneous systems. Additional complexity includes increased salt precipitation in high-permeability zones due to lower Ca enhanced by capillary-induced imbibition of saline water from low-permeability zones. Tortuous flow paths can also emerge, further exacerbating pressure build-up. These novel characterizations can assist practitioners in designing mitigation strategies for injectivity impairment in large-scale operations.

Keywords: Geological CO_2 storage, salt precipitation, injectivity impairment, capillary number, reservoir heterogeneity.

Introduction

Geological CO_2 storage (GCS) is a mature technology for the mitigation of greenhouse gases with successful demonstration in 26 projects across different geological settings worldwide (Krevor et al., 2023). The ability to sustain a desired injection rate over time, so-called injectivity, underpins the deployment of CO_2 storage technology on a large scale. Injectivity can suffer due to poor reservoir quality of the storage formation, either at the outset or over time, if the pore space becomes blocked by other mechanisms. Salt precipitation falls into the latter category, whereby water vaporizes into the dry injected CO_2, leaving salt deposits that block the pore space and reduce permeability. The result is pressure build-up that can approach unsafe levels, causing a technical risk to the project. Experience gained with storage in saline aquifers has shown that many projects experience no noticeable injectivity problems (e.g., Sleipner storage project). However, salt precipitation has been documented in a few field cases (Ketzin (Baumann et al., 2014) and Aquistore (Talman et al., 2020)) and required treatment in one notable case, i.e., Snøhvit CCS project (Pawar et al., 2015). As treatment is costly, a reliable means for assessing the risk of salt precipitation is necessary in planning industrial-scale storage projects. It should be noted that salt precipitation in fractures that penetrate the caprock can block potential leakage pathways, thereby decreasing risk (Ji et al., 2025; Nooraiepour et al., 2018).

Comprehensive knowledge of the mechanisms controlling salt precipitation and injectivity impairment has been obtained through laboratory-scale studies of CO_2 injection into centimeter-scale core plugs or millimeter-scale micromodels. The reader is referred to the extensive literature review by Miri & Hellevang (2016) and Cui et al. (2023). In bench-scale studies, constant total flow conditions are established by pumping CO_2 at the inlet and allowing

fluid to escape at the outlet. Observations of salt precipitation are well documented in these experiments and indicate that most salt is precipitated at the inlet (Bacci et al., 2011; Oh et al., 2013; Peysson et al., 2014). Factors such as salinity, temperature, pressure, and rock properties are important for determining the amount of salt precipitation (Chao et al., 2024; Zamani, Oldenburg, et al., 2024; Zamani, Shokri, et al., 2024). The resulting increase in pressure drop between the inlet and outlet is used to infer a reduction in permeability, up to several orders of magnitude in some studies (Bacci et al., 2011; He et al., 2019; Muller et al., 2009; Ott et al., 2015; Tang et al., 2015). These studies also established a clear impact of capillarity: slower flow rates led to increased salt precipitation due to capillary-driven backflow, as observed in microfluidic experiments (Akindipe et al., 2021; Dabrowski et al., 2025; Ho & Tsai, 2020; Yan et al., 2025). Numerical modeling studies have shown that, to properly investigate near-wellbore processes such as salt precipitation and to resolve the effects of different controlling parameters, high-resolution meshes are required in the vicinity of the injection well (Moridis et al., 2023; Wapperom et al., 2022).

Simulation studies are fundamental for interpreting experimental observations, and several studies (Ott et al., 2015; Sokama-Neuyam et al., 2023) have validated existing models. However, larger-scale simulations are essential to uncover insights beyond the bench scale. Modeling salt precipitation in three-dimensional (3D) storage reservoirs is necessary to assess the impact of: (1) radial flow conditions, (2) gravity, and (3) larger length scales. Under radial-flow conditions, the flow velocity decreases as the radial distance from the injection well increases. At the same time, gravity causes buoyant CO_2 to rise upwards, displacing the resident brine downward. The full 3D effect leads to a spatial variation of the force balance, with viscous force prevailing near the wellbore and a transition to gravity and capillary dominance occurring tens to hundreds of meters into the reservoir (Kelly & Mathias, 2018; Perez-Perez & Berthelot, 2025).

The ultimate impact of 3D flow effects on salt precipitation is difficult to quantify due to the increasing number of sensitivities involved. Simulation studies have confirmed that capillary number is essential for field-scale salt precipitation through a clear dependence on injection rate and formation permeability (Kim et al., 2012; Landa-Marbán et al., 2024; Piao et al., 2018; Pruess & Müller, 2009). The dependence on permeability implies that heterogeneity should play a role, but no studies have systematically explored this. The petrophysical properties, especially capillary entry pressure, significantly influence the salt precipitation driven by capillarity. Although water becomes immobile within fully developed dry-out regions, capillary entry pressure remains important at the advancing dry-out front. In a recent study, the capillary entry pressure was shown to evolve dynamically due to a reduction in porosity and permeability caused by salt precipitation, leading to enhanced capillary imbibition and increased salt precipitation (Chen et al., 2024).

With respect to gravity, it is more challenging to quantify the added influence from the available literature. A few studies (Kim et al., 2012; Pruess & Müller, 2009) have shown significant gravitational impacts, whereby salt precipitation becomes localized toward the bottom of the reservoir as CO_2 rises to the top of the formation. This localization phenomenon is linked to lower injection rates and higher permeability, i.e., low capillary numbers, but the increased buoyancy of lower-density CO_2 also appears to play a role. Other studies report the heterogeneous salt distribution (Guyant et al., 2015; Norouzi et al., 2021; Oh et al., 2013) while others report that salt precipitates uniformly (Ott et al., 2015; Zeidouni et al., 2009). None of the above-mentioned studies has reported the information needed to define the factors that determine salt localization and how pressure build-up is affected.

In summary, despite several field-scale simulation studies on salt precipitation, obtaining enough general insight to characterize and predict the risk of injectivity loss for any given combination of factors remains challenging. A general characterization should account for all

properties that affect viscous, capillary, and gravity forces, e.g., injection rate, formation permeability, petrophysical properties of the storage formation, and the thermophysical properties of CO_2, which depend dynamically on temperature and pressure. Furthermore, for more realistic settings, we must consider the influence of heterogeneity, in which one would expect local differences in the strength of capillary force due to changes in permeability. And finally, realistic operation of injection wells that adapt to the local pressure increase caused by salt precipitation and shift injection away from blocked zones.

In this study, we develop a new approach to characterizing salt precipitation and subsequent impact on injectivity. Three non-dimensional groups are formulated - Capillary number (Ca), Bond number (Bo), and Gravity number (Gr) - that encompass the reservoir, fluid and petrophysical properties, as well as the injection rate, which together govern salt precipitation at field scale. We employ fine-scale simulations using TOUGH2-ECO2N to quantify total salt precipitation, salt localization, and bottom-hole pressure build-up as a function of these non-dimensional groups. Here, fine-scale refers to the use of locally refined spatial discretization near the wellbore to resolve strong gradients in pressure and saturation, as well as salt precipitation. We begin with a simplified homogeneous reservoir model to establish a general baseline for capillary and gravity controls on salt precipitation. Next, we add more complexity to the model by introducing a realistic wellbore and reservoir heterogeneity. Through this structured approach, we thoroughly investigate and quantify the interactions among the forces governing salt precipitation dynamics in CO_2 storage contexts. The findings from this study are intended to support the industry in evaluating safe operational conditions and investigating preventive strategies.

Model description

Conceptual Model

Three regions are formed when less viscous, dry CO_2 is injected into a saline aquifer, schematically illustrated in Figure 1. Farthest away from the wellbore is Region I, which represents the undisturbed region that remains close to the initial conditions of the aquifer in terms of fluid saturation. Upon the commencement of injection, CO_2 displaces brine and establishes a region of two-phase flow (Region II), where the CO_2 is fully saturated with respect to water vapor. Over time, a third region evolves closest to the inlet, also known as the *dry-out region*, where residual brine has been completely evaporated by continuous injection of dry CO_2, leaving behind precipitated salt.

CO_2 flow dynamics and salt precipitation are governed by three fundamental forces: viscous, capillary, and gravity (Krevor et al., 2023). Viscous force, driven by pressure gradients or flow rates, is strongest near the wellbore and diminishes deeper into the reservoir (Regions II and III). It is possible to have sufficiently large viscous effects to overcome processes such as capillary backflow or gravitational override.

On the other hand, capillary pressure is a diffusive force that seeks to disperse two fluids. Capillarity is an intrinsic property of the fluid-rock system. In a water-wet reservoir, capillary force can induce brine to flow counter-currently from Region II to Region III (the dry-out zone) via thin water films on rock grains. Capillary backflow allows considerable salt to be transferred from other regions and possibly precipitated in Region III. Systems with higher capillarity, i.e., low-permeability systems or significantly water-wet systems, tend to have greater potential for backflow when the viscous force is negligible.

Finally, the gravity force is controlled mainly by density differences between CO_2 and brine, while reservoir anisotropy governs how buoyance effects manifest through vertical and horizontal transmissibility. Due to the dependence of CO_2 density on temperature and pressure, spatial and temporal variations in gravitational effects within the reservoir are expected. As CO_2

migrates farther from the wellbore (Regions I and II), gravity plays an increasingly prominent role. CO_2 will tend to rise to the top of the reservoir, while capillary force will retain it in a vertical zone below, called the capillary transition zone.

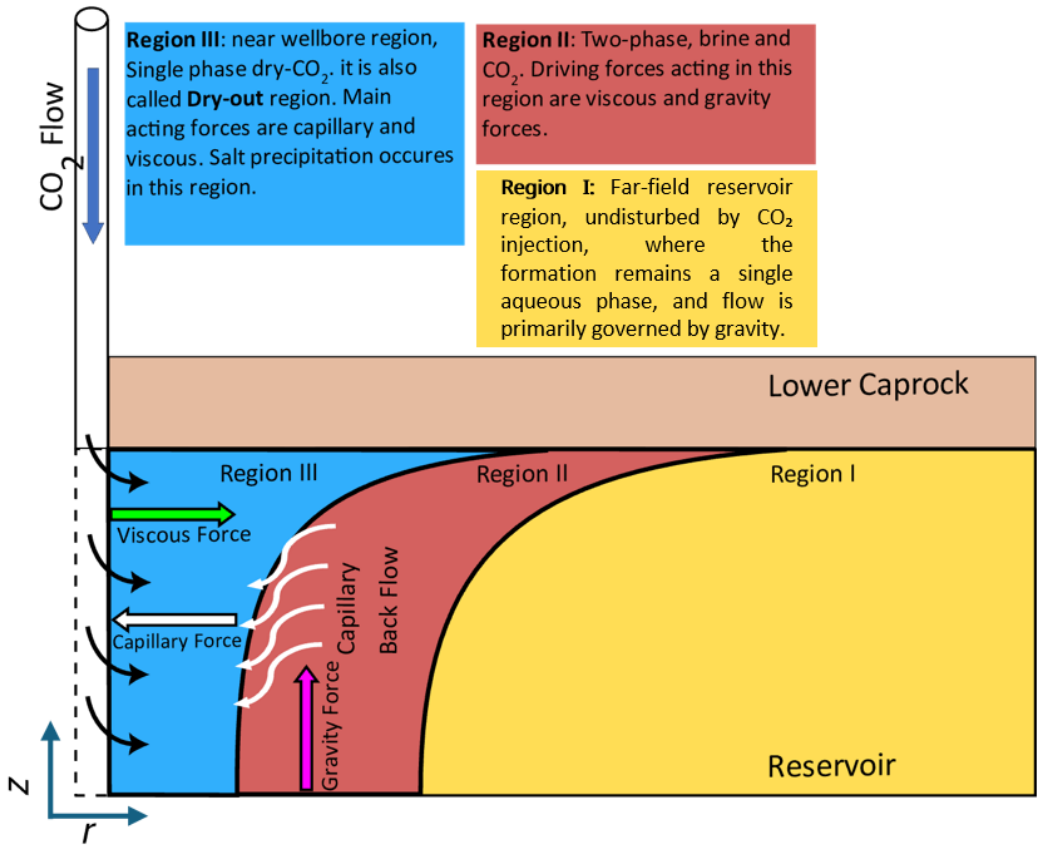

Figure 1: Schematic illustration of the formed flow zone and acting forces during axisymmetric CO_2 injection into a saline aquifer.

Dimensionless groupings are valuable for evaluating the relative significance of these three forces on the onset, extent, and amount of salt precipitation. The Ca number determines the balance between viscous and capillary forces. The Bo number indicates the ratio of gravity to capillary forces. The Gr number captures the balance between the gravity and viscous forces. Various formulations are used in the literature to describe the Ca number (Guo et al., 2022), where we adopt the approach of (Kopp et al., 2009), and Equation 2 and Equation 3 for Bo and Gr numbers, respectively.

$$Ca = \frac{Viscous\ Force}{Capillary\ Force} = \frac{\mu_{CO_2}.v_{cr}.l_{crh}}{K.P_{cr}} \quad \text{Equation 1}$$

$$Bo = \frac{Gravitational\ Force}{Capillary\ Force} = \frac{(\rho_w - \rho_{CO_2}).g.l_{crv}}{P_{cr}} \quad \text{Equation 2}$$

$$Gr = \frac{Bo}{Ca} = \frac{(\rho_w - \rho_{CO_2}).g.l_{crv}.K}{\mu_{CO_2}.v_{cr}.l_{crh}} \quad \text{Equation 3}$$

Key parameters include v_{cr} (Darcy velocity), P_{cr} (entry capillary pressure), with gravitational acceleration coefficient, g rounded to 10 [m/s^2]. The CO_2 viscosity (μ_{CO_2}) and density (ρ_{CO_2}) are 6.35e-5 [Pa.sec] and 743 [kg/m^3], respectively, while water density, ρ_w, is 1000 [kg/m^3]. The thermophysical properties of CO_2 and brine used in this study correspond to the initial reservoir conditions, with a temperature of 60 °C, and a pressure of 21.3 MPa. K is the reservoir absolute permeability. The horizontal critical length (l_{crh}) used to compute the Ca number is

set to 1 meter, representing a near-wellbore reference scale for evaluating viscous pressure gradients. This length represents a near-wellbore reference scale selected a priori and applied consistently across all cases to enable comparative analysis. While the spatial extent of viscous-capillary force competition may vary depending on fluid, reservoir, and operational properties, this interaction is primarily expressed within the near-wellbore region, typically over the first few meters from the injection point. Changing the characteristic length would alter the absolute value of the calculated Ca number; however, because the same reference length is applied consistently across all cases, the relative trends and classification in Ca–Gr space remain unchanged. Conversely, in calculating the Bo number, the vertical critical length (l_{crv}) is set to the reservoir thickness, reflecting the vertical scale over which buoyancy force acts.

Numerical Model

This study employs TOUGH2 for all simulations; however, DuMux (Egberts et al., 2018) or OPM Flow (Landa-Marbán et al., 2024) are also suitable choices. TOUGH2 solves the coupled mass and energy conservation equations using a fully implicit finite-volume formulation on a discretized spatial grid, with nonlinear systems solved via Newton-Raphson iteration. The ECO2N module (Pruess, 2004) is utilized as the equation-of-state (EOS) package to model H_2O–NaCl–CO_2 mixtures and provides accurate phase property calculations within the relevant temperature, pressure, and salinity ranges. All simulations are transient and performed under isothermal conditions. Adaptive time stepping is employed, controlled by convergence criteria on mass and energy residuals.

Salt is treated as a dissolved component in the aqueous phase. Salt precipitation occurs automatically when local brine salinity exceeds the solubility limit due to water evaporation during CO_2 injection. Precipitated salt reduces porosity and permeability through the implemented porosity-permeability relationship; no additional empirical precipitation trigger or user-defined threshold is imposed. Relative permeability and capillary pressure (Pc) are described using the van Genuchten formulation. Details on the numerical model setup and input parameters are summarized in the Supporting Information (Table S1 and Figure S1).

To ensure meaningful comparison across cases with different injection rates, the total injected mass of CO_2 is kept constant by adjusting the injection duration accordingly. A reference case injects CO_2 at 11 kg/s continuously for one year. For cases in which the injection rate is increased or decreased by an order of magnitude, the injection duration is shortened or extended proportionally such that the same total mass of CO_2 is injected in all simulations. Each simulation terminates once the prescribed injection period is complete.

We note two modeling choices. First, conventional capillary pressure models typically do not describe the evolution of Pc at saturations below the irreducible water saturation, where dry-out and salt precipitation occur. The log-linear extension of the conventional curve closely matches the available data (Webb, 2000). However, in this study, we implement a threshold capillary pressure equal to 10^7 Pa on the standard van-Genuchten curve as a suitable alternative. Second, the relationship between salt-induced porosity loss and permeability reduction is highly sensitive to the pore-size distribution (Shiran et al., 2024), among other factors. In this study, we employed the tubes-in-series model, implemented within TOUGH2, to characterize this correlation. The model is defined by two parameters, ϕ_r and Γ, with $\Gamma = 0.8$ was used in this study. Unless stated otherwise, a residual porosity fraction of $\Phi_r = 0.8$ was used in the simulations. A lower value ($\Phi_r = 0.1$), corresponding to a 90% loss of the initial porosity before permeability vanishes, was applied only in selected sensitivity cases to avoid premature reservoir blockage and allow continued simulation of salt precipitation patterns. Results obtained using $\Phi_r = 0.1$ are therefore not directly comparable to those generated with $\Phi_r = 0.8$, as the lower residual porosity significantly alters the permeability–porosity relationship and

injectivity response. Further discussion regarding these modelling choices is provided in the Supporting Information (Figure S2).

Physical Model

The reservoir model in this study features a 2D axisymmetric geometry located at a depth of 2100 meters with a thickness of 44 meters, and a radius (R) of 10 km. The upper and lower boundaries are defined as no-flow boundaries, representing impermeable caprock and base rock conditions. CO_2 is injected at the left boundary at a prescribed constant mass injection rate. The right boundary is defined by a constant-pressure condition equal to the initial reservoir pressure, ensuring that the model represents a semi-infinite reservoir domain without artificial boundary effects. All simulations were performed under isothermal conditions, at 60 ºC. Porosity is assumed constant at 0.2, while the absolute permeability (K) ranges from 15 to 1500 mD, with a base-case value of 150 mD. The reservoir contains brine with a salinity of 15 wt% NaCl.

The model discretization scheme is presented in Figure 2. Vertically, the domain is divided into 22 uniformly spaced grid cells, each with a thickness of 2 meters. Radially, the model is discretized using a non-uniform grid system, with finer grid cells near the wellbore (10 cm to accurately capture near-wellbore processes) that progressively increase in size with radial distance into the reservoir. Salt concentration profiles are typically shown along the bottom and top boundaries of the model domain, indicated by blue and green lines, respectively. The top profile (green line in Figure 2) is extracted at 1 meter below the reservoir top, while the bottom profile (blue dashed line in Figure 2) is extracted 1 meter above the reservoir bottom.

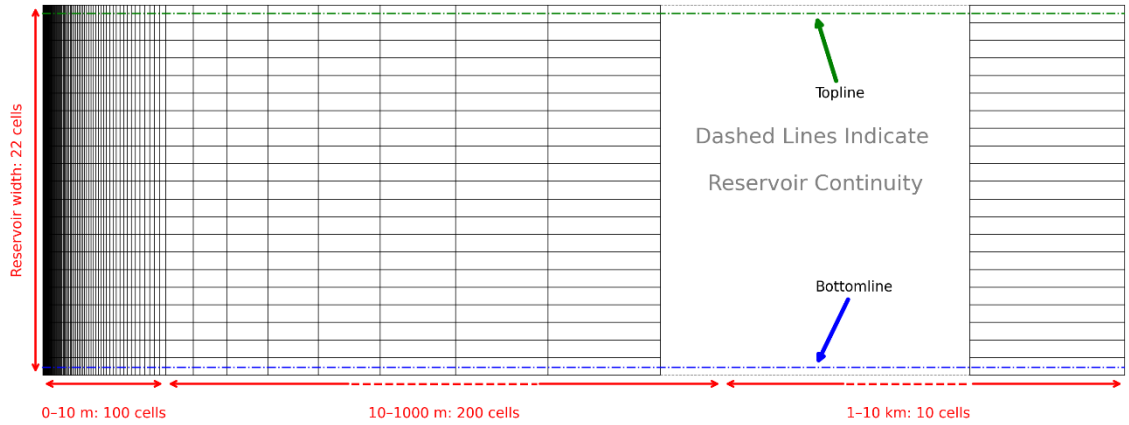

Figure 2: Schematic illustration of model dimensions and the mesh used for numerical simulation.

Characterization of capillary-viscous-gravity effects in 3D field-scale models

We perform a series of test cases to build a systematic understanding of salt precipitation in a 3D field-scale setting. Simulations are first performed for a homogenous reservoir to facilitate interpretation of the results in terms of the Ca, Bo, and Gr dimensionless numbers. The test cases are grouped according to the dominant force balance investigated, with a base case, capillary-controlled cases, and gravity-controlled cases. A complete description of all cases and parameters is provided in Table S2.

Capillary number test case

The relative strength of the capillary and viscous forces influences salt precipitation behavior, as previously observed in one-dimensional core-flood experiments in the absence of gravity (Akindipe et al., 2021; Dabrowski et al., 2025; Ho & Tsai, 2020; Yan et al., 2025). Here, we

extend this analysis to the field scale by systematically varying the Ca number. This is achieved by independently varying the injection rate (11, 1.1, 0.11 kg/s) and permeability (15, 150, 1500 mD), resulting in a total of 9 test cases.

Gravity number test case

Gravitational effect is important at the field scale and competes with viscous force in controlling gravity override and vertical fluid segregation. The impact of fluid segregation on salt precipitation is investigated by testing a range of gravity numbers (Gr). Eight additional cases are derived by varying entry capillary pressure (Pcr = 0.002, 0.2, and 20 kPa) and gravitational acceleration (g = 0, 1, and 10 m/s²). Although values of g < 10 m/s^2 are not physical, varying g is used here as a numerical device to span a range of the gravity force; equivalent gravity numbers could alternatively be achieved under realistic conditions by varying parameters such as the CO_2-brine density difference. Note that a reduced injection rate (1.1 kg/s) is used in these cases to maintain realistic input variables across all test cases.

Results

The results are first presented for homogeneous reservoir models to establish the role of capillary, viscous and gravity forces using Ca–Gr analysis. The framework is then extended to more realistic scenarios by including wellbore effects and reservoir heterogeneity, and their implications for salt precipitation and injectivity are discussed.

Ca number analysis

The effect of Ca number on salt saturation profiles has been studied in detail using the Base case and Ca1_0.1R, representing high- and low-Ca conditions, respectively (the injection rate is reduced by one order of magnitude in Ca_0.1R). In this study, salt concentration refers to the volumetric fraction of pore space occupied by precipitated solid salt formed by brine evaporation during CO_2 injection. Salt concentration profiles extracted along the topmost and bottommost horizontal layers of the reservoir are shown in Figure 3-a. The locations of the top and bottom lines have been shown in Figure 2.

Four key features are observed: (1) a reduction in viscous force (lower Ca) significantly increases salt precipitation near the wellbore; (2) the salt distribution shifts from being relatively uniform in the Base Case to becoming localized away from the wellbore in Ca1_0.1R; (3) for the low-Ca case, salt precipitation is higher along the bottom layer than along the top layer, whereas the two profiles are nearly identical in the high-Ca case; and (4) a higher Ca number (Base case) leads to a greater lateral extent of salt precipitation (approximately 5 m), compared to about 2 m for the low-Ca case.

The associated gas saturation and salt precipitation within the 25 m region near the wellbore, illustrated in Figure 3 b-e, indicate that low-Ca (Ca1_0.1R) exhibits stronger gravitational override and fluid segregation than the Base Case. Reduced viscous force enhances capillary-driven brine backflow toward the dry-out region near the bottom of the reservoir, resulting in increased salt precipitation. Localized salt precipitation can act as a flow barrier, forcing CO_2 upward and enhancing gravity override. This localization is not observed in the Base Case, indicating that it arises from the combined dominance of capillary and gravity forces relative to viscous force. Although the Bo number remains greater than unity in both cases, our analysis indicates that capillary-driven brine backflow and associated salt precipitation near the wellbore are primarily controlled by the Ca number, whereas Bo mainly governs the large-scale vertical segregation away from the injection point.

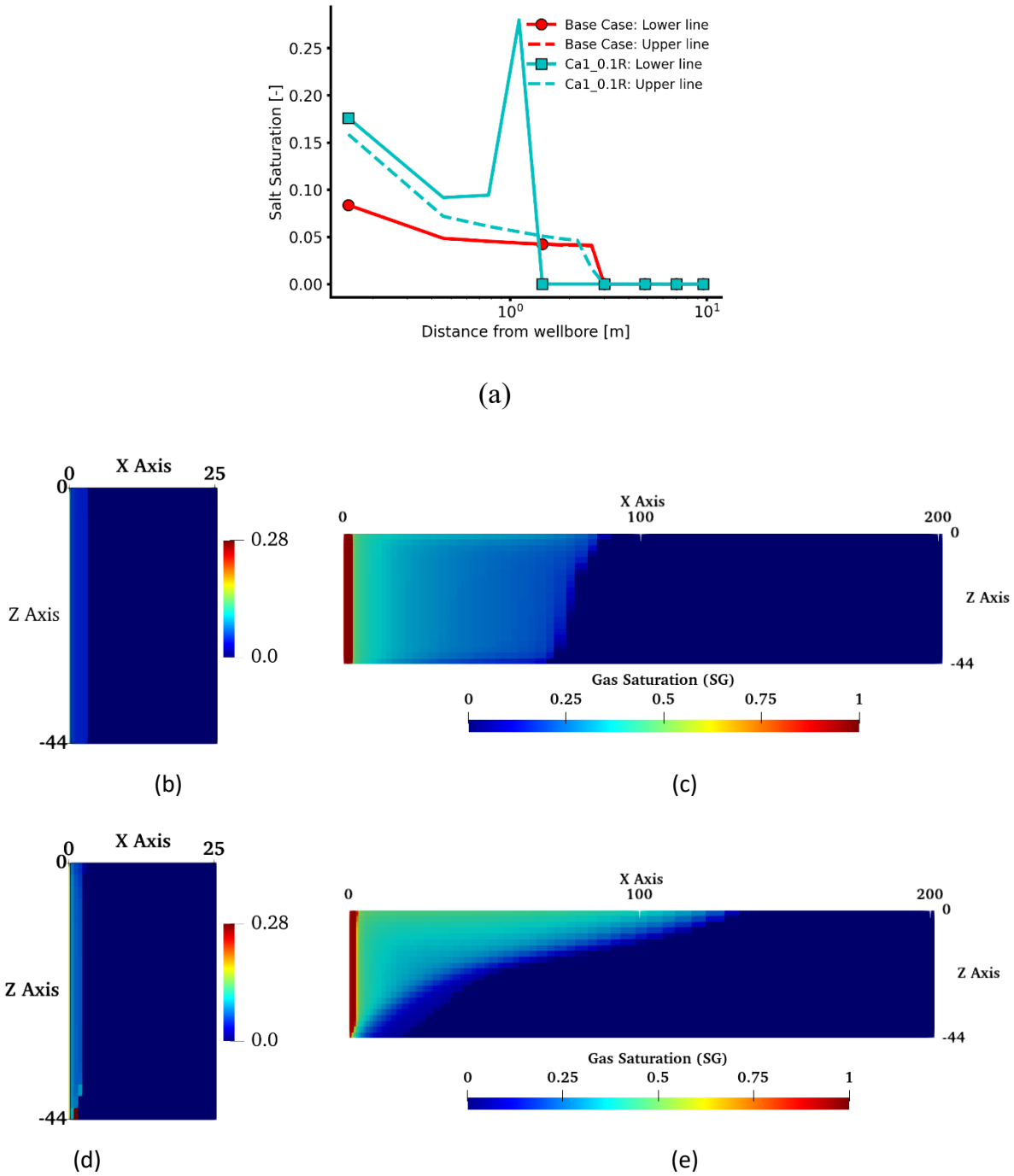

Figure 3: (a) Salt saturation profiles along the bottommost (lower line) and topmost (upper line) horizontal layers of the reservoir for the Base Case and Ca1_0.1R. Distance is measured radially from the wellbore. (b) Base Case: salt precipitation within 25 m of the wellbore, (c) Base Case: Gas saturation distribution (d) Ca1_0.1R: salt precipitation within 25 m of the wellbore, (e) Ca1_0.1R: Gas saturation distribution.

Comparison of salt concentration profiles of different Ca test cases (Figure 4) reveals important observations. First, we observe that salt precipitation patterns are identical for a given Ca number. It is worth noting that these identical salt profiles also correspond to identical Gr and Bo numbers. Second, salt precipitation at the inlet increases as Ca decreases, due to increased capillary backflow at lower Ca. The lowest Ca tested (Ca = 0.05) leads to complete blockage of the inlet. In all cases, observed trends with Ca are consistent with behavior previously studied in one-dimensional systems (Akindipe et al., 2021; Miri & Hellevang, 2016; Ott et al., 2015).

Examining three-dimensional effects reveals that salt concentration profiles exhibit a clear dependence on both Ca and Gr, while remaining independent of Bo, which is constant across all cases shown in Figure 4. Further study of the Bo number is shown in Figure S5. Across all cases, decreasing Ca leads to increased salt precipitation near the wellbore, reflecting enhanced capillary-driven brine backflow under reduced viscous force. At the same time, increasing Gr promotes the development of localized salt precipitation away from the wellbore, indicating a stronger influence of gravity-driven fluid segregation. Referring to the formulations of Ca and Gr, both parameters are associated with a reduction in viscous dominance, albeit through different mechanisms. The most pronounced behavior is observed in cases where low Ca and high Gr occur simultaneously (blue curves), for which both near-wellbore salt accumulation and strong localization away from the wellbore develop. In these cases, salt precipitation becomes extensive across the near-wellbore region, resulting in an almost uniform, high-magnitude salt concentration profile.

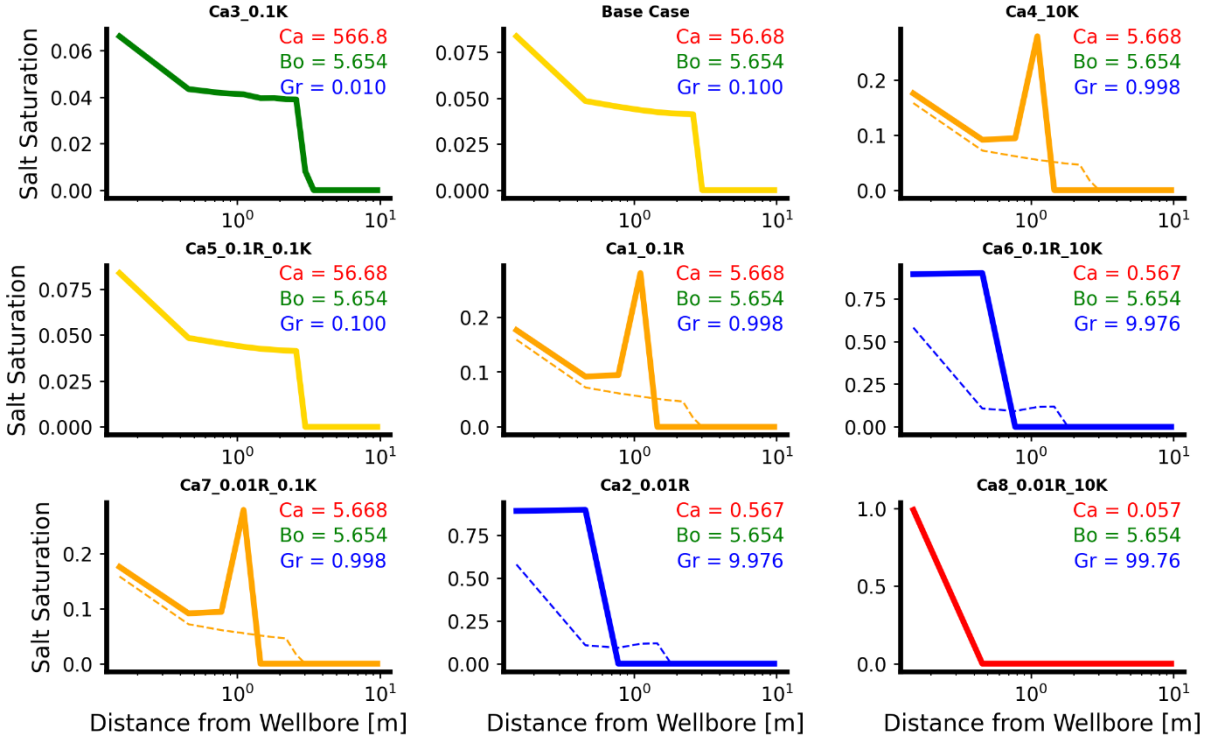

Figure 4: Comparison of salt saturation profiles along the bottommost (thick line) and topmost (thin dashed line) layers of the reservoir. Corresponding Ca, Bo, and Gr numbers are mentioned in each plot. Note that in some cases, the profiles along the top and bottom lines are indistinguishable

Synthesis of results in Ca-Gr space

In the previous test cases, we clearly identified the influence of the Ca on the magnitude of salt precipitation near the wellbore. However, the dominant force governing the development of localized salt precipitation away from the wellbore could not be isolated based on that test design alone. To address this limitation, we extend the analysis by jointly examining the effects of the Gr and Ca. In addition, a dedicated sensitivity analysis was performed in which the Bo was varied independently. These results demonstrate that Bo does not control either near-wellbore salt precipitation or the development of localized salt precipitation away from the wellbore. To create a more complete picture of the Gr-Ca space, we perform additional simulations described earlier (rf. Table S2) covering a wider range of parameters. We also collect available results from the literature (Kim et al., 2012), that indicate salt localization in 3D field-scale simulations. Details on the estimates of Ca, Bo, and Gr from the literature and the cases used here are provided in Table S3.

Figure 5 synthesizes all results from the present study, together with available literature data, by mapping the occurrence vs. non-occurrence of salt localization in the Gr-Ca parameter space. In this work, salt precipitation is classified as 'localized' when a distinct salt accumulation away from the wellbore inlet is formed, driven by vertical fluid segregation, rather than salt precipitation confined to the near-wellbore dry-out zone. Salt localization (triangles) is observed for cases with relatively high Ca and intermediate Gr values, approximately within the region $0.2 < Gr < 1$ and $Ca > 1$, while non-localized behavior occurs outside this region. These boundaries should be interpreted as indicative regime limits rather than sharp thresholds, as the classification is based on the actual Ca and Gr values associated with each case (see Table S3)

The results indicate that localized salt precipitation is associated with conditions where the gravity effect becomes comparable relative to viscous force, allowing vertical fluid segregation to develop, while capillary force is not sufficiently strong to suppress this segregation. Under such conditions, capillary back flow cannot prevent the formation of dry-out zones away from the wellbore, leading to localized salt precipitation deeper in the reservoir.

Two additional regimes are identified: a capillary-dominated regime ($Ca < 1$), characterized by severe salt precipitation near the inlet (circles) and a viscous-dominated regime ($Ca > 1$ and $Gr < 0.2$) where salt precipitation remains relatively uniform and limited in magnitude across the reservoir height (squares).We note two important points. First, the combined Gr-Ca controls on salt localization are an additional effect to the previously reported impact of Ca on salt precipitation at the inlet. One may consider these processes independent of each other, unless Ca is so low that it leads to total blockage at the inlet at an early stage. Second, we exclude cases in the region $Gr > 1$ and $Ca > 1$ in this analysis as this would entail unphysical reservoir properties.

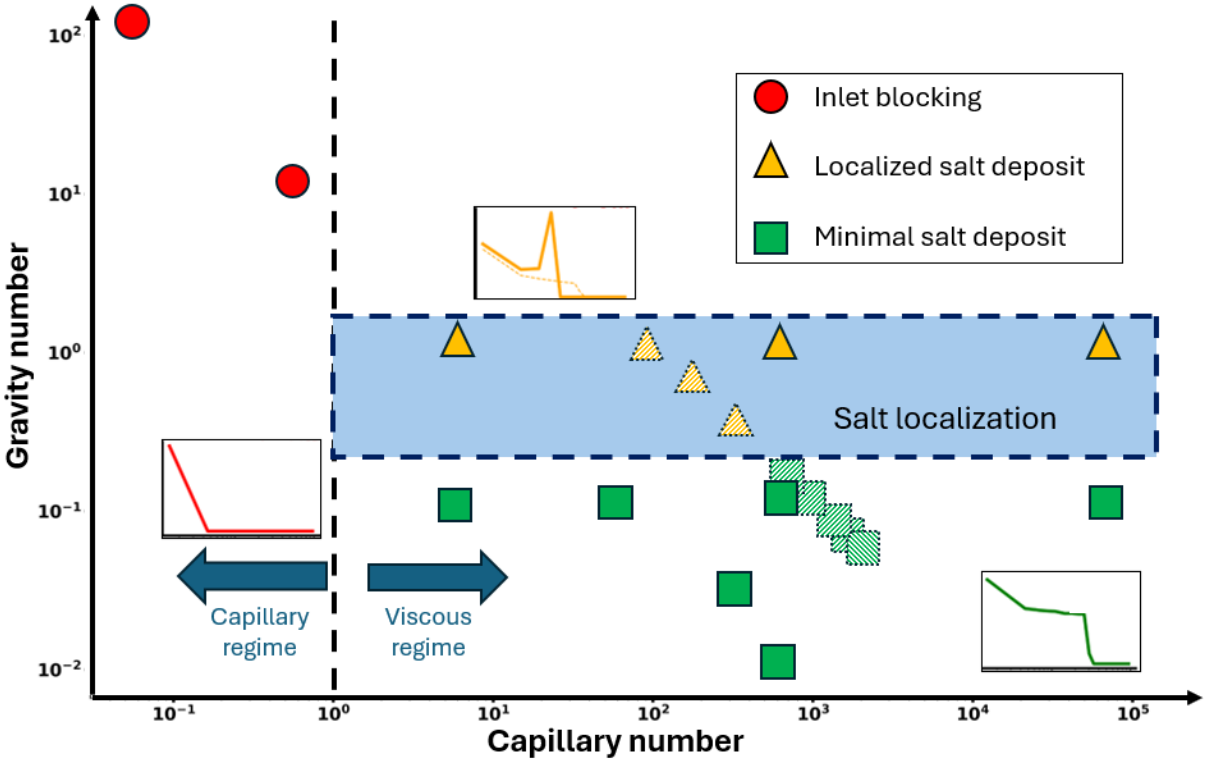

Figure 5: Ca versus Gr number map illustrating salt precipitation behavior. Triangles indicate cases with localized salt precipitation, circles represent inlet blocking, and squares correspond to minimal or non-localized salt precipitation. Results from Kim et al. (2012) are shown with dashed shading. The blue region highlights the parameter range in which salt localization is observed.

Application to realistic reservoir conditions

The Ca-Gr characterization for homogeneous systems is extended here. Heterogeneity introduces spatial variability in Ca and Gr numbers through variations in the formation's permeability and capillary pressure. Local Ca and Gr values can also be impacted by differences in injection along sections of the well that experience lower resistance to flow. This section studies the additional impact of heterogeneity and variable wellbore/inlet flow on salt precipitation.

All cases in this section use a wellbore model that allows injection rates to vary with the local pressure gradient along different vertical sections of the inlet, which adds complexity to the flow conditions compared to the uniform flow conditions assumed in the previous test cases. Following the methodology of Pruess & Müller (2009), we explicitly incorporate the wellbore model into the TOUGH2. In this approach, a single cell is designated as the wellbore, and the total injection rate is dynamically distributed among the adjacent cells along the vertical extent of the well according to local phase mobility and pressure gradients. This approach represents a single vertical well interacting with multiple reservoir layers. Whereas, in the uniform injection cases, the total injection rate is evenly divided among the reservoir cells along the vertical extent of the model, such that each cell receives the same prescribed injection rate, independent of local mobility and pressure conditions.

To assess the impact of wellbore coupling, we compare a uniform-injection base case with a wellbore-coupled case (Case1_W), in which all injection cells are replaced by a single wellbore cell. As shown in Figure 6, although the lateral extent of CO_2 saturation remains similar between the two cases, the distribution of salt precipitation near the wellbore differs markedly due to the redistribution of injection rates (Figure 7). Under uniform injection, salt precipitation is vertically uniform along the inlet, whereas inclusion of the wellbore leads to broader salt accumulation toward the top of the reservoir.

Salt saturation profiles extracted along the bottom and top layers (Figure 7-a and b) show that, in the wellbore-coupled case, the bottom layer develops a distinct salt accumulation peak away from the wellbore, indicating localized salt precipitation not observed under uniform injection. This behavior is consistent with enhanced gravity-driven segregation when viscous force is reduced. In contrast, the top layer exhibits a broader lateral extent of salt precipitation due to increased local injection rates.

Analysis of the time evolution of layer-specific injection rates (Figure 7-c and d) shows that, with wellbore coupling, injection rates decrease over time in the bottom layer and increase in the top layer as flow redistributes according to local pressure gradients and mobility. In the bottom layer, reduced injection rates lower the viscous force while the gravitational force remains unchanged, increasing the Gr number and promoting salt localization. Conversely, increased injection rates in the top layer enhance viscous force and increase Ca, leading to reduced salt precipitation and wider lateral spreading.

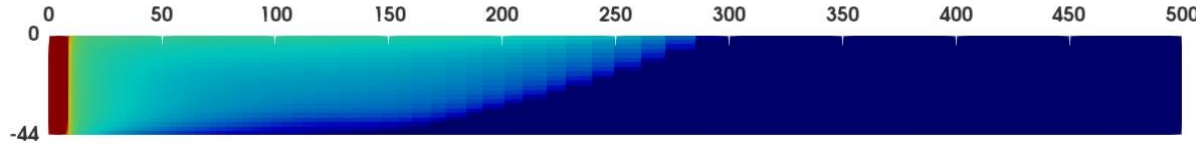

(a)

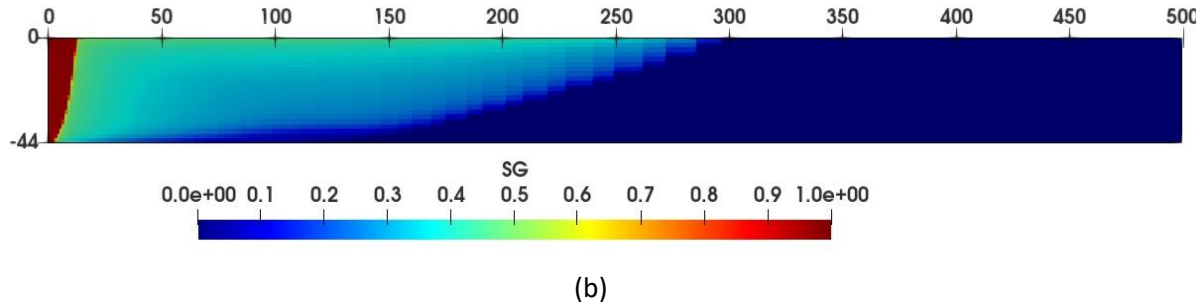

(b)

Figure 6: Gas saturation distribution in the reservoir: (a) uniform distribution and (b) including wellbore.

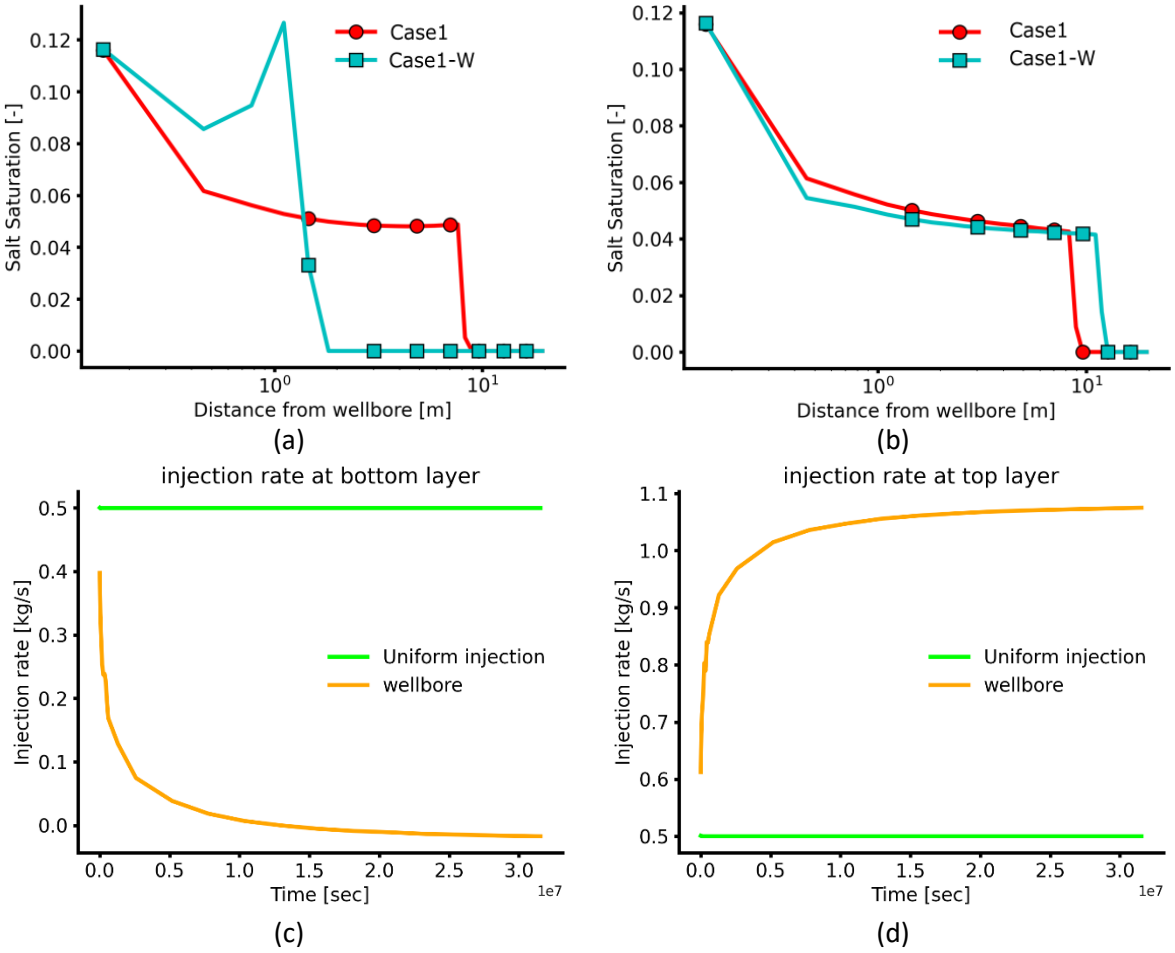

Figure 7: Effect of coupling wellbore-reservoir on salt precipitation and injection rates: a-b show salt precipitation profiles along the bottommost and topmost layers of the reservoir, c-d show the corresponding time evolution of the injection rates

Realistic test case set-up

The first case (4B_Layered) introduces three permeability layers (15, 150, and 1500 mD) into the homogeneous base case reported in the Ca number analysis. For this case, a single capillary pressure curve corresponding to the base permeability (K = 150 mD) is applied uniformly to all layers, as shown by the middle curve in Figure 8. The second case (4C_Equil) is identical to 4B_Layered but uses an equivalent homogeneous permeability defined as the arithmetic average of the layered permeabilities. An additional case (4D_Layered_JF) considers heterogeneity in the capillary pressure function as an added effect for the layered permeability case (4B_Layered). In this case, the capillary pressure for each layer is scaled by the Leverett

J-function (Equation 4), where $\sqrt{\frac{K_{base}}{K_{layer}}}$ is used to reflect the permeability differences, with resulting curves shown in Figure 8.

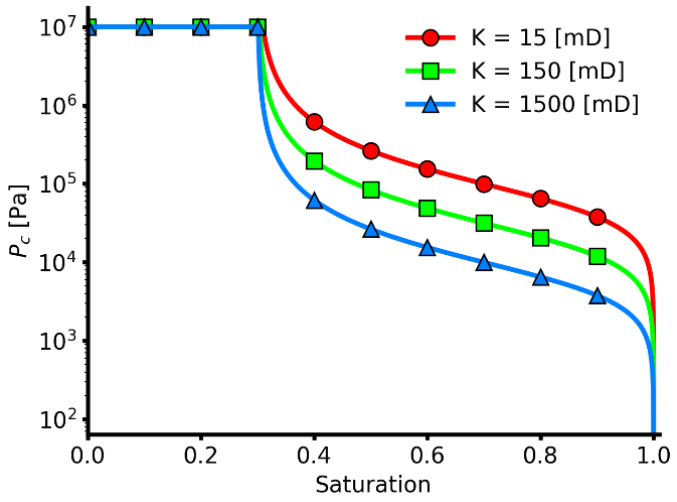

Figure 8: Capillary pressure curves used in 4D_Layered_JF for different layers with different permeabilities.

Although the Leverett J-function scales the magnitude of capillary pressure as a function of permeability and porosity, the irreducible water saturation (S_{lir} = 0.30) was kept constant across all layers. This choice was made to avoid altering the amount of available brine and dissolved salt, which would directly affect the total salt precipitation. By keeping S_{lir} fixed, the analysis isolates the impact of capillary pressure magnitude on flow redistribution and salt precipitation patterns, without introducing artificial differences in salt availability between layers.

$$P_c = \sqrt{\frac{\phi_{layer} K_{base}}{\phi_{base} K_{layer}}}\, P_c^0(S_w) \qquad \text{Equation 4}$$

The final case (4E_random) employs a random permeability distribution to investigate the influence of flow pathways between layered and randomly distributed permeability fields. The random permeability field is generated by assigning permeability values selected from three discrete values (15, 150, and 1500 mD), with spatial distribution controlled by a horizontal (radial) correlation length of 10 meters, while no vertical correlation is imposed. The permeability fields for layered and random case are shown in Figure 9. For the layered and random cases, the horizontal length scale of the permeability variability is significantly larger and significantly smaller, respectively, than the simulated domain.

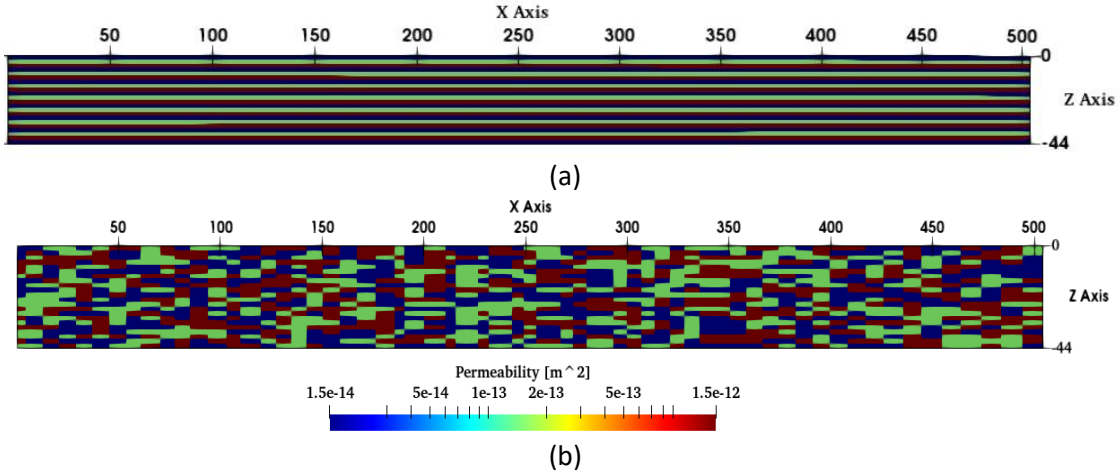

Figure 9: Permeability distribution within the reservoir for (a) layered cases, where permeability varies stratigraphically, and (b) randomly distributed permeability.

Results for layered permeability with and without capillary heterogeneity

Figure 10 compares the layered permeability case without capillary heterogeneity (4B_Layered) and the layered case with capillary heterogeneity introduced via the Leverett-J function (4D_Layered_JF). In Figure 10-a and b, we observe that the pattern of CO_2 flow and resulting salt precipitation is affected by the contrast in high- to low-permeability layers. CO_2 flows more easily in the higher-permeability layers, which promotes increased flow in the wellbore model. The additional impact of heterogeneity in capillary properties for the layered system (4D_Layered_JF) shows an overall consistent trend compared to the layered case without capillary heterogeneity (4B_Layered), but with a greater lateral extent of the CO_2 plume. This behavior can be attributed to the lower capillary entry pressure in the high-permeability layer after modification using the Leverett-J function.

The combination of higher permeability and variable wellbore flow results in higher flow rates in the higher permeability layers in both cases (Figure 10-c and d). Here, we see that flow rates in high-k layers are 10 times higher than in low-k layers. We note that this nominal flow rate increase is outweighed by a two orders-of-magnitude difference in permeability between high- and low-k layers. Thus, the Ca number in the high-permeability layers is significantly lower compared to the lower-permeability layers. As expected from our prior Ca-number analysis, more salt precipitation occurs in the high-k layers.

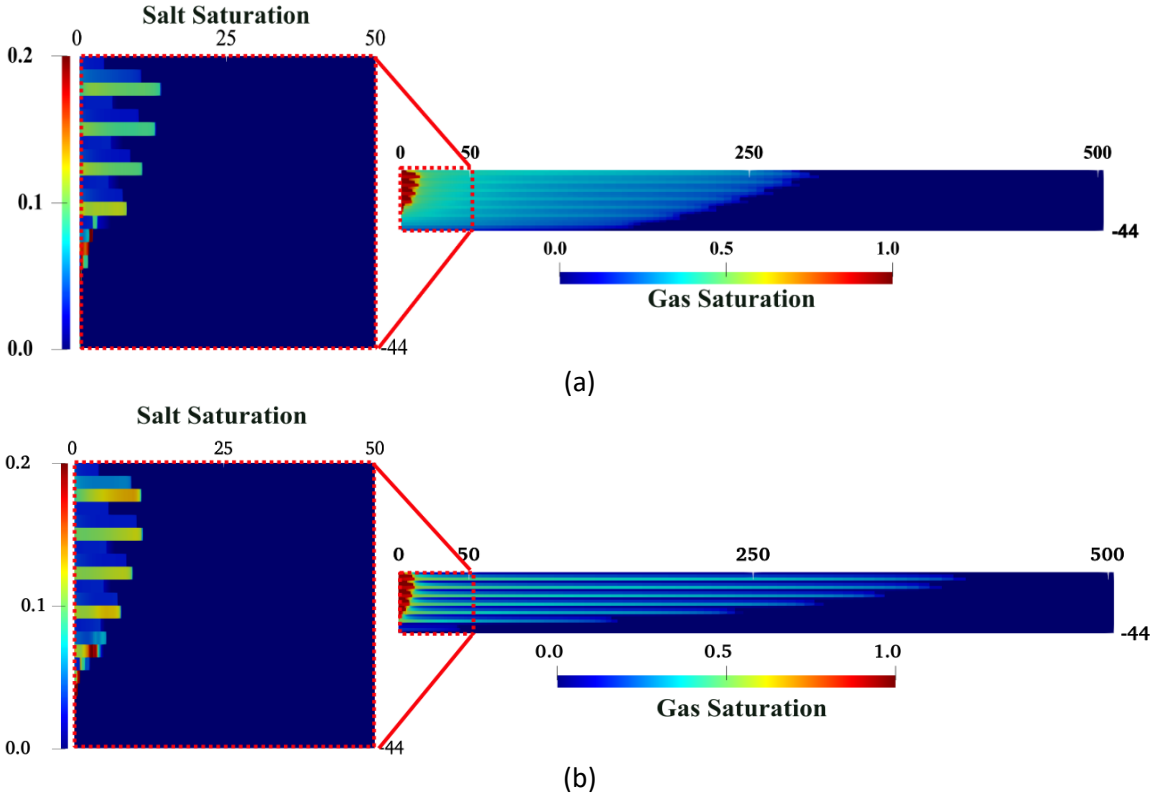

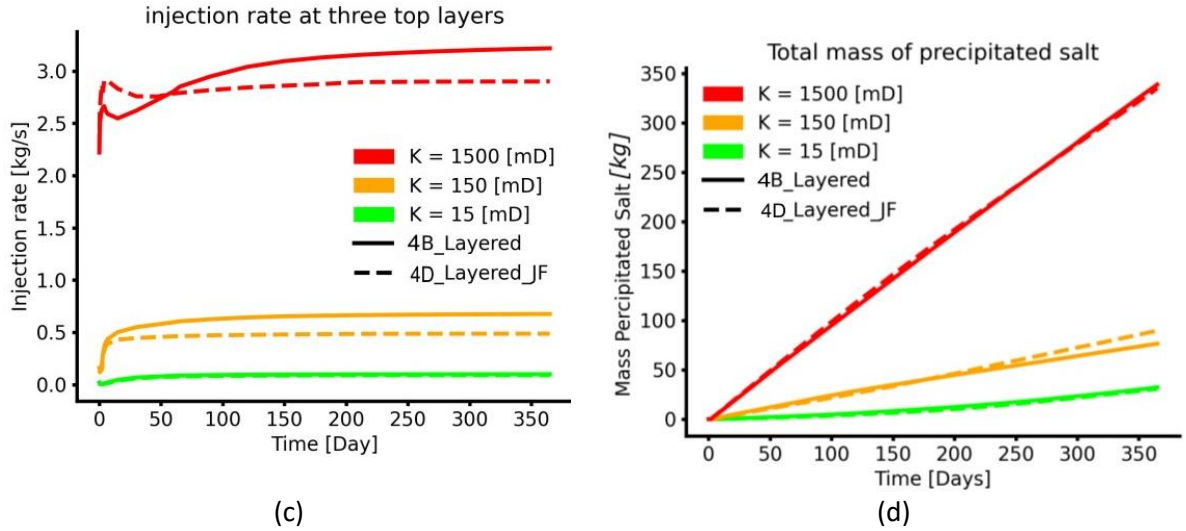

Figure 10: CO_2 saturation along the model and salt distribution within the zoomed near-wellbore region (50 m) for (a) 4B_Layered and (b) 4D_Layered_JF. (c) Comparison of flow rate distribution within the top three layers for 4B_Layered (solid) and 4D_Layered_JF (dashed line). (d) Comparison of the total mass of precipitated salt across layers with different permeabilities.

Both layered cases exhibit some salt localization in deeper high-k layers, which we attribute to Gr-Ca numbers in the regime shown in Figure 5. We observe that the case with capillary heterogeneity additionally leads to salt localization towards the top of the reservoir. Drawing from earlier discussion, this result indicates that capillary heterogeneity leads to a greater influence of gravity in the viscous-dominated regime. We recall that as salt precipitates preferentially in the high-k layers, the permeability declines and flow rates decrease (Figure 10-c) and flow is diverted into the lowest permeability layers as a result (due to the wellbore model). The larger reduction in flow rate in the high-permeability layers in the case of capillary heterogeneity leads to a stronger decrease in local Ca and an increase in local Gr, shifting the system into the Gr–Ca regime associated with salt localization.

The differences in local flow dynamics and associated salt precipitation due to modification of capillary properties have only a minor impact on total salt precipitation (Figure 10-d). The total amount of salt precipitation remains nearly unchanged (456 kg in 4D_Layered_JF and 447 kg in 4B_Layered). There is a notable increase in the amount of salt observed in the middle layer (from 76 kg in 4B_Layered to 90 kg in 4D_Layered_JF), even though the capillary properties remain the same. One would expect larger differences in total salt precipitation with varying capillary properties, given the local differences observed in Figure 10-b. It is likely due to the ability of the well to divert flow in response to permeability changes, which has the effect of balancing out local differences. It can be interpreted as a tendency for the system to spread salt precipitation more uniformly. Confirmation of this link would require additional study beyond the scope of this work.

Results of the random permeability case

CO_2 injection with salt precipitation into a random permeability field (cf. Figure 9-b) results in a more vertically distributed saturation front, with fewer preferential flow pathways of the layered cases. As a result, the CO_2 plume extends laterally over a shorter distance (Figure 11-a) compared to the layered cases (Figure 10-a). Notably, salt precipitation near the wellbore exhibits a different pattern, becoming highly localized in certain regions (Figure 11-b). As observed in previous cases, salt precipitation still occurs predominantly in high-permeability areas (Figure 11-c).

Over the one-year injection period, the total salt precipitation in 4E_random reaches approximately 449 kg, closely matching the total amounts in 4B_Layered (447 kg) and

4D_Layered_JF (456 kg). However, the distribution of salt across different permeability regions is more uneven: 312 kg precipitate in the high-permeability zones, 122 kg in the middle-permeability zones, and only 14 kg in the lowest-permeability regions (Figure 11-c). While calculating the Ca and Gr numbers for individual cells presents challenges, the overall trend persists: high-permeability areas correspond to lower Ca numbers, which results in higher salt precipitation. On the other hand, as injection continues, higher salt precipitation in high permeable regions reduces the permeability, diverts flow into other regions, increases Gr number and consequently shifts salt-preciption pattern from uniform to localized precipitation, as observed in Figure 11-b. This is consistent with earlier findings.

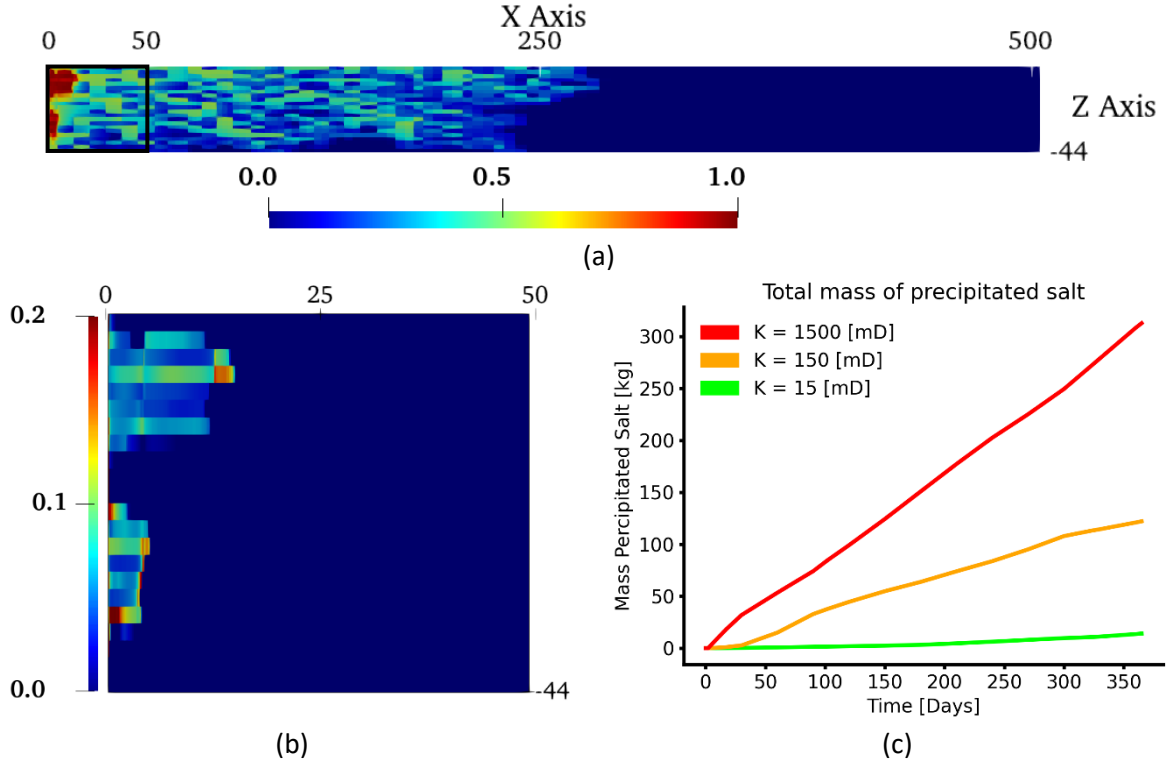

Figure 11: (a) gas saturation distribution; (b) salt precipitation in a zoomed area of 50 meters near the wellbore; (c) Accumulated salt precipitation over time in different layers

Discussion

This study provides new insights into the complex interactions among viscous, capillary, and gravity forces governing salt precipitation during CO_2 injection using dimensionless parameters. It is well established through core flooding experiments and 1D numerical simulations that the competition between viscous and capillary forces is the dominant factor controlling salt precipitation at the inlet. Our study confirms that the Ca-dependency for salt precipitation at the inlet in 1D linear systems also holds in 3D radial models (Ott et al. ,2014, Miri & Hellevang, 2016 and Akindipe et al., 2021). Furthermore, our study provides additional insights into gravitational and heterogeneity effects that can only be captured in 3D field-scale simulations and are inherently absent in 1D systems.

First, gravity plays a significant role alongside viscous and capillary forces, influencing the vertical spatial distribution of salt precipitation not observed in core floods. Second, radial flow conditions cause a gradual reduction in the viscous force relative to capillary and gravity forces with increasing distance from the wellbore. Third, reservoir heterogeneity introduces further complexity by locally enhancing or suppressing different forces, thereby altering their relative strength of the forces over time and space.

A key observation from our study is that localized salt precipitation can occur when the gravitational force dominates. Importantly, under specific conditions, the amount of precipitated salt inside the reservoir can exceed that at the inlet. An internal barrier builds up, driving CO_2 upward and reducing reservoir sweep. While previous numerical studies have reported this phenomenon, its governing mechanisms and the conditions under which different salt localizations emerge had not been systematically investigated. Our novel findings demonstrate that a combination of Ca and Gr is needed to predict and manage salt precipitation patterns more generally. The Ca number controls salt precipitation near the wellbore, and the Gr number controls the occurrence of localized salt precipitation. The proposed approach has been tested against results from the literature, confirming its applicability under different reservoir conditions.

Applying this approach in heterogeneous reservoirs is challenging, as calculating Ca and Gr values for each region is difficult due to spatial variations in permeability and flow paths. However, our results show that the general trends of salt precipitation with respect to Ca and Gr remain consistent with those in homogeneous systems. The total salt precipitation is nearly identical among different heterogeneous settings, as it primarily depends on the amount of dry CO_2 that contacts brine. However, the spatial distribution of precipitated salt and consequently injectivity loss is controlled by different factors, including flow dynamics and reservoir properties, especially capillarity and heterogeneity. Capillary force plays a significant role in the amount of salt precipitation in the vicinity of the wellbore through the capillary backflow mechanism.

Injection pressure profiles from different cases suggested that an equivalent homogeneous medium can effectively reproduce the pressure response of layered heterogeneous models, while it is not applicable for the random heterogeneous model (See Figure S7). In a random permeability field, flow paths are generally more tortuous. When salt blocks the high-permeability zones, CO_2 flow is forced into the low-permeability zone, thereby increasing injection pressure.

Proper wellbore modeling, particularly its coupling with reservoir flow, is another critical factor influencing salt precipitation. Flow distribution along the reservoir height is naturally governed by pressure gradients, with flow preferentially following the least-resistant pathways (i.e., high-permeability zones). In high-permeability layers, lower capillary numbers promote greater salt precipitation, redirecting flow into low-permeability layers. Therefore, the combined effect of reduced transmissibility in high-permeability layers and increased flow through low-permeability regions leads to higher injection and drawdown pressures. This behavior has been confirmed by wellbore imaging from the Aquistore project in Canada (Talman et al., 2020), providing field-scale observations which can support our findings.

The main findings of this study may be affected by other secondary assumptions and modeling choices, such as isothermal conditions. Ignoring temperature variation leasds to ignoring variation in CO_2 properties, which could affect the gravity number (density) and capillary number (viscosity). The temperature variation may occur as CO_2 flows through surface facilities, along the wellbore, and across perforations. Such transient thermal effects have been addressed in numerical studies (Zamani, Oldenburg, et al., 2024) and documented through field observations, e.g., at the Aquistore site (Rangriz Shokri et al., 2021). Strong thermal changes induced by injection are not common in GCS except in the case of injection into depleted reservoirs (Zamani, Rangriz Shokri, et al., 2024).

The injectivity analysis can be highly sensitive to the choice of permeability-porosity relationship (Zhang & Liu, 2016). Relevant data are scarce, and more systematic experimental measurements should be conducted on representative reservoir rocks to improve understanding of permeability reduction due to salt precipitation.

Future work could build on the present findings by quantitatively linking salt precipitation patterns to injectivity metrics under more realistic settings. In particular, comparing injectivity indices for cases with localized salt precipitation versus more uniformly distributed salt precipitation would provide valuable insight into operational consequences. Such analysis would require experimentally constrained porosity–permeability relationships to accurately capture permeability impairment due to salt precipitation, as well as a systematic exploration of gravitational and capillary effects under transient conditions. Extending the present framework in this direction would help translate regime-based insights into predictive tools for injection performance and risk management in large-scale CO_2 storage operations.

Conclusion

This study successfully characterized the viscous, capillary, and gravity controls on salt precipitation patterns during CO_2 injection. Three distinct regimes are identified in Ca-Gr dimensionless space which help differentiate between flow conditions that lead to severe blocking in a capillary-dominated regime versus formation of localized salt barriers within the reservoir in a gravity-dominated regime. The results show that the injectivity impairment due to salt precipitation can be minimized when the Ca number is high *and* Gr number is low. These findings hold generally for heterogeneous reservoirs, with additional small-scale complexity emerging as heterogeneity increases. Future experimental investigations are needed to better constrain capillary pressure behavior in CO_2-brine systems under dry-out conditions ($Sw < Sw_{ir}$), particularly to validate and refine Pc modelling approaches used during salt precipitation.

Using dimensionless parameters such as Ca and Gr is beneficial to summarize complex interactions and it highlights that proper consideration of both reservoir (e.g. heterogeneity, capillary pressure, temperature and pressure) and operational conditions (e.g. injection rate) is essential for a successful project design. For example, high-permeability reservoirs, which may initially seem favorable for CO_2 injection, can still experience severe injectivity impairement if injection rate is not kept sufficiently high.

Within the Ca–Gr framework, a transition from localized to more uniformly distributed salt precipitation can be expected if operational conditions shift the system toward a viscous-dominated regime. For example, increasing the injection rate raises the Ca and decreases Gr, strengthening viscous force relative to capillary and gravity forces, which reduces capillary backflow and suppresses gravity-driven segregation. Similarly, injecting CO_2 at a lower temperature decreases fluid density contrasts, thereby reducing the Gr and weakening buoyancy effects. Under such conditions, salt precipitation is more likely to remain confined near the wellbore or be distributed more uniformly across the reservoir thickness rather than forming localized barriers deeper in the formation. This illustrates how operational adjustments can potentially mitigate salt localization and associated injectivity impairment.

These findings can be applied in industrial project design in developing optimized injection strategies, including dynamic flow rate adjustments to mitigate the risk of injectivity impairment in large-scale CO_2 storage operations.

Acknowledgement

The authors acknowledge funding from the Centre of Sustainable Subsurface Resources (CSSR), grant nr. 331841, supported by the Research Council of Norway, research partners NORCE Norwegian Research Centre and the University of Bergen, and user partners Equinor ASA, Harbour Energy, Sumitomo Corporation, Earth Science Analytics, GCE Ocean Technology, and SLB Scandinavia.

Supporting Information

Supporting_information.pdf: a detailed description of the numerical model and associated input parameters, additional analysis of capillary pressure effects on injectivity, the impact of Bond Number (Bo) on salt concentration profile, parameters extracted from Kim et al. (2012) with corresponding Ca, Bo, and Gr values.

References

Akindipe, D., Saraji, S., & Piri, M. (2021). Salt precipitation during geological sequestration of supercritical CO2 in saline aquifers: A pore-scale experimental investigation. *Advances in Water Resources*, *155*, 104011. https://doi.org/10.1016/J.ADVWATRES.2021.104011

Bacci, G., Korre, A., & Durucan, S. (2011). Experimental investigation into salt precipitation during CO2 injection in saline aquifers. *Energy Procedia*, *4*, 4450–4456. https://doi.org/10.1016/J.EGYPRO.2011.02.399

Baumann, G., Henninges, J., & De Lucia, M. (2014). Monitoring of saturation changes and salt precipitation during CO2 injection using pulsed neutron-gamma logging at the Ketzin pilot site. *International Journal of Greenhouse Gas Control*, *28*, 134–146. https://doi.org/10.1016/J.IJGGC.2014.06.023

Chao, L., Jialin, Y., Zihao, Z., Chaofu, F., Songze, L., Nanxin, Y., Cen, C., & Hun, L. (2024). Implications and problems of research on salt precipitation during CO2 injection into saline sandstone: a comprehensive review. *Environmental Earth Sciences 2024 83:14*, *83*(14), 427-. https://doi.org/10.1007/S12665-024-11733-9

Chen, X.-S., Hu, R., Zhou, C.-X., Xiao, Y., Yang, Z., & Chen, Y.-F. (2024). *Capillary-Driven Backflow During Salt Precipitation in a Rough Fracture*. https://doi.org/10.1029/2023WR035451

Dabrowski, K., Nooraiepour, M., Masoudi, M., Smulski, R., Hellevang, H., & Nagy, S. (2025). *Understanding Salt Precipitation Dynamics during CO2 Injection into Saline Aquifers using Microfluidic Experiments*. *2025*(1), 1–5. https://doi.org/10.3997/2214-4609.202510377

Egberts, P. J. P., Nair, R., & Twerda, A. (2018). Salt Precipitation in the Near Well Bore Region of Gas Wells. *Proceedings - SPE International Symposium on Formation Damage Control*, *2018-February*. https://doi.org/10.2118/189541-MS

Guo, H., Song, K., & Hilfer, R. (2022). A Brief Review of Capillary Number and its Use in Capillary Desaturation Curves. *Transport in Porous Media*, *144*(1), 3–31. https://doi.org/10.1007/S11242-021-01743-7/TABLES/3

Guyant, E., Han, W. S., Kim, K. Y., Park, M. H., & Kim, B. Y. (2015). Salt precipitation and CO2/brine flow distribution under different injection well completions. *International Journal of Greenhouse Gas Control*, *37*, 299–310. https://doi.org/10.1016/J.IJGGC.2015.03.020

He, D., Jiang, P., & Xu, R. (2019). Pore-Scale Experimental Investigation of the Effect of Supercritical CO2 Injection Rate and Surface Wettability on Salt Precipitation. *Environmental Science and Technology*, *53*(24), 14744–14751. https://doi.org/10.1021/ACS.EST.9B03323/SUPPL_FILE/ES9B03323_SI_010.AVI

Ho, T. H. M., & Tsai, P. A. (2020). Microfluidic salt precipitation: implications for geological CO2 storage. *Lab on a Chip*, *20*(20), 3806–3814. https://doi.org/10.1039/D0LC00238K

Ji, T., Haghi, A. H., Jiang, P., Chalaturnyk, R., & Xu, R. (2025). Capillary-Driven Transport and Precipitation of Salt in Heterogeneous Structures During Carbon Sequestration. *Geophysical Research Letters*, *52*(13), e2024GL114388. https://doi.org/10.1029/2024GL114388;CTYPE:STRING:JOURNAL

Kelly, H. L., & Mathias, S. A. (2018). Capillary processes increase salt precipitation during CO2 injection in saline formations. *Journal of Fluid Mechanics*, *852*, 398–421. https://doi.org/10.1017/JFM.2018.540

Kim, K. Y., Han, W. S., Oh, J., Kim, T., & Kim, J. C. (2012). Characteristics of Salt-Precipitation and the Associated Pressure Build-Up during CO 2 Storage in Saline Aquifers. *Transport in Porous Media*, *92*(2), 397–418. https://doi.org/10.1007/S11242-011-9909-4/METRICS

Kopp, A., Class, H., & Helmig, R. (2009). Investigations on CO2 storage capacity in saline aquifers: Part 1. Dimensional analysis of flow processes and reservoir characteristics. *International Journal of Greenhouse Gas Control*, *3*(3), 263–276. https://doi.org/10.1016/J.IJGGC.2008.10.002

Krevor, S., De Coninck, H., Gasda, S. E., Ghaleigh, N. S., De Gooyert, V., Hajibeygi, H., Juanes, R., Neufeld, J., Roberts, J. J., & Swennenhuis, F. (2023). nature reviews earth & environment Subsurface carbon dioxide and hydrogen storage for a sustainable energy future. *Nature Reviews Earth & Environment* |, *4*, 102–118. https://doi.org/10.1038/s43017-022-00376-8

Landa-Marbán, D., Zamani, N., Sandve, T. H., & Gasda, S. E. (2024). Impact of Intermittency on Salt Precipitation During CO2 Injection. *Society of Petroleum Engineers - SPE Norway Subsurface Conference, BERG 2024*. https://doi.org/10.2118/218477-MS

Miri, R., & Hellevang, H. (2016). Salt precipitation during CO 2 storage-A review. *International Journal of Greenhouse Gas Control*, *51*, 136–147. https://doi.org/10.1016/j.ijggc.2016.05.015

Moridis, G. J., Reagan, M. T., Huang, T., & Blasingame, T. A. (2023). Practical Aspects and Implications of Long-Term CO2 Sequestration in Saline Aquifers Using Vertical Wells. *SPE Latin American and Caribbean Petroleum Engineering Conference Proceedings*, *2023-June*. https://doi.org/10.2118/213168-MS

Muller, N., Qi, R., Mackie, E., Pruess, K., & Blunt, M. J. (2009). CO2 injection impairment due to halite precipitation. *Energy Procedia*, *1*(1), 3507–3514. https://doi.org/10.1016/J.EGYPRO.2009.02.143

Nooraiepour, M., Fazeli, H., Miri, R., & Hellevang, H. (2018). Effect of CO2 Phase States and Flow Rate on Salt Precipitation in Shale Caprocks - A Microfluidic Study. *Environmental Science and Technology*, *52*(10), 6050–6060. https://doi.org/10.1021/ACS.EST.8B00251/SUPPL_FILE/ES8B00251_SI_003.AVI

Norouzi, A. M., Babaei, M., Han, W. S., Kim, K. Y., & Niasar, V. (2021). CO2-plume geothermal processes: A parametric study of salt precipitation influenced by capillary-driven backflow. *Chemical Engineering Journal*, *425*, 130031. https://doi.org/10.1016/J.CEJ.2021.130031

Oh, J., Kim, K. Y., Han, W. S., Kim, T., Kim, J. C., & Park, E. (2013). Experimental and numerical study on supercritical CO2/brine transport in a fractured rock: Implications of mass transfer, capillary pressure and storage capacity. *Advances in Water Resources*, *62*, 442–453. https://doi.org/10.1016/J.ADVWATRES.2013.03.007

Ott, H., Roels, S. M., & de Kloe, K. (2015). Salt precipitation due to supercritical gas injection: I. Capillary-driven flow in unimodal sandstone. *International Journal of Greenhouse Gas Control*, *43*, 247–255. https://doi.org/10.1016/J.IJGGC.2015.01.005

Pawar, R. J., Bromhal, G. S., Carey, J. W., Foxall, W., Korre, A., Ringrose, P. S., Tucker, O., Watson, M. N., & White, J. A. (2015). Recent advances in risk assessment and risk management of geologic CO2 storage. *International Journal of Greenhouse Gas Control*, *40*, 292–311. https://doi.org/10.1016/J.IJGGC.2015.06.014

Perez-Perez, A., & Berthelot, A. (2025). Assessing Well Impairment Due to Halite Precipitation in Saline Aquifers During CO2 Injection Scenarios. *Society of Petroleum Engineers - SPE Europe Energy Conference and Exhibition, EURO 2025*. https://doi.org/10.2118/225572-MS

Peysson, Y., André, L., & Azaroual, M. (2014). Well injectivity during CO2 storage operations in deep saline aquifers—Part 1: Experimental investigation of drying effects, salt precipitation and capillary forces. *International Journal of Greenhouse Gas Control*, *22*, 291–300. https://doi.org/10.1016/J.IJGGC.2013.10.031

Piao, J., Han, W. S., Choung, S., & Kim, K. Y. (2018). Dynamic Behavior of CO2 in a Wellbore and Storage Formation: Wellbore-Coupled and Salt-Precipitation Processes during Geologic CO2 Sequestration. *Geofluids*, *2018*(1), 1789278. https://doi.org/10.1155/2018/1789278

Pruess, K. (2004). The TOUGH Codes—A Family of Simulation Tools for Multiphase Flow and Transport Processes in Permeable Media. *Vadose Zone Journal*, *3*(3), 738–746. https://doi.org/10.2136/VZJ2004.0738

Pruess, K., & Müller, N. (2009). Formation dry-out from co2 injection into saline aquifers: 1. effects of solids precipitation and their mitigation. *Water Resources Research*, *45*(3). https://doi.org/10.1029/2008WR007101

Rangriz Shokri, A., Talman, S., Chalaturnyk, R. J., & Nickel, E. (2021). *On the Temporal Evolution of Non-Isothermal Injectivity Behaviour at an Active CO2 Injection Site*. OnePetro. https://dx.doi.org/

Shiran, B. S., Sadaak, B., Solbakken, J., Toigo, C., & Zamani, N. (2024). Impact of Salt Precipitation on Porosity-Permeability Correlations: Implications for CO2 Storage. *5th EAGE Global Energy Transition Conference and Exhibition, GET 2024*, *2024*(1), 1–5. https://doi.org/10.3997/2214-4609.202421174/CITE/REFWORKS

Sokama-Neuyam, Y. A., Yusof, M. A. M., Owusu, S. K., Darkwah-Owusu, V., Turkson, J. N., Otchere, A. S., & Ursin, J. R. (2023). Experimental and theoretical investigation of the mechanisms of drying during CO2 injection into saline reservoirs. *Scientific Reports 2023 13:1*, *13*(1), 1–11. https://doi.org/10.1038/s41598-023-36419-3

Talman, S., Shokri, A. R., Chalaturnyk, R., & Nickel, E. (2020). Salt Precipitation at an Active CO2 Injection Site. *Gas Injection into Geological Formations and Related Topics*, 183–199. https://doi.org/10.1002/9781119593324.CH11

Tang, Y., Yang, R., Du, Z., & Zeng, F. (2015). Experimental Study of Formation Damage Caused by Complete Water Vaporization and Salt Precipitation in Sandstone Reservoirs. *Transport in Porous Media*, *107*(1), 205–218. https://doi.org/10.1007/S11242-014-0433-1/FIGURES/13

Wapperom, M., Lyu, X., & Voskov, D. (2022). Accurate modeling of near-wellbore effects induced by supercritical CO2 injection. *European Conference on the Mathematics of Geological Reservoirs 2022, ECMOR 2022*, *2022*(1), 1–13. https://doi.org/10.3997/2214-4609.202244092/CITE/REFWORKS

Webb, S. W. (2000). A simple extension of two-phase characteristic curves to include the dry region. *Water Resources Research*, *36*(6), 1425–1430. https://doi.org/10.1029/2000WR900057

Yan, L., Niftaliyev, R., Voskov, D., & Farajzadeh, R. (2025). Dynamics of salt precipitation at pore scale during CO2 subsurface storage in saline aquifer. *Journal of Colloid and Interface Science*, *678*, 419–430. https://doi.org/10.1016/J.JCIS.2024.08.265

Zamani, N., Oldenburg, C. M., Solbakken, J., Aarra, M. G., Kowollik, P., Alkan, H., Amro, M. M., Nassan, T. H., Estrada, J. K. P., & Burachok, O. (2024). CO 2 flow modeling in a coupled wellbore and aquifer system: Details of pressure, temperature, and dry-out. *International Journal of Greenhouse Gas Control*, *132*, 104067. https://doi.org/10.1016/j.ijggc.2024.104067

Zamani, N., Rangriz Shokri, A., Chalaturnyk, R. J., Gasda, S., & Berenblyum, R. (2024). Significance of the Joule-Thomson Cooling Effect for Geological CO2 Storage in Depleted Gas Reservoirs. *SSRN Electronic Journal*. https://doi.org/10.2139/SSRN.5070337

Zamani, N., Shokri, A. R., Chalaturnyk, R., Solbakken, J., & Berenblyum, R. (2024). *Modelling of Non-Isothermal Effects on Salt Precipitation during Geological CO2 Storage*. *2024*(1), 1–5. https://doi.org/10.3997/2214-4609.202410834/CITE/REFWORKS

Zeidouni, M., Pooladi-Darvish, M., & Keith, D. (2009). Analytical solution to evaluate salt precipitation during CO2 injection in saline aquifers. *International Journal of Greenhouse Gas Control*, *3*(5), 600–611. https://doi.org/10.1016/J.IJGGC.2009.04.004

Zhang, S., & Liu, H. H. (2016). Porosity–permeability relationships in modeling salt precipitation during CO2 sequestration: Review of conceptual models and implementation in numerical simulations. *International Journal of Greenhouse Gas Control*, *52*, 24–31. https://doi.org/10.1016/J.IJGGC.2016.06.013

Supporting Information

Unraveling Salt Precipitation Mechanisms in CO_2 Storage Reservoirs: Insights into Dominant Driving Forces

*Nematollah Zamani[1], David Landa-Marbán[1], Tor Harald Sandve[1], Sarah E. Gasda[1,2] **

[1] Department of Energy and Technology,NORCE Norwegian Research Centre AS, Nygårdstangen, NO-5838, Bergen, Norway

[2] Department of Physics and Technology, University of Bergen, Allégaten 55, 5007, Bergen, Norway

* Corresponding author:

E-mail: nematollah.Zamani@norceresearch.no

Numerical model

This study employs TOUGH2, a versatile numerical simulator designed for the fluid flow of multiple components and phases. The formulation and implementation are extensively detailed in Pruess (2004) [1]. TOUGH2 has been coupled by the ECO2N package, which serves as an equation of state (EOS) module. ECO2N accurately calculates fluid properties of individual phases and H_2O–NaCl–CO_2 mixtures, aligning closely with experimental values within the specified temperature, pressure, and salinity of interest (10°C ≤ T ≤ 110°C; P ≤ 600 bar; salinity up to full halite saturation) [2].

The *van Genuchten* equations are used to model relative permeabilities and capillary pressure in this context, and there are succinctly summarized in the following equations:

$$k_{rl} = \begin{cases} \sqrt{S^*}\left\{1-\left(1-[S^*]^{1/m}\right)^m\right\}^2, & S_l < S_{ls} \\ 1, & S_l \geq S_{ls} \end{cases} \quad \text{Equation 1}$$

$$k_{rg} = \begin{cases} 1-k_{rl}, & S_{gr} = 0 \\ \left(1-\hat{S}\right)^2\left(1-\hat{S}^2\right), & S_{gr} > 0 \end{cases} \quad \text{Equation 2}$$

$$S^* = \frac{S_l - S_{lr}}{1-S_{lr}}, \quad \text{Equation 3}$$

$$\hat{S} = \frac{(S_l - S_{lr})}{1-S_{lr}-S_{gr}}, \quad \text{Equation 4}$$

$$P_c = P_0\left([S^*]^{-1/\lambda}-1\right)^{1-\lambda}, \quad \text{Equation 5}$$

In the above formulations S_l is the liquid saturation, S_{lr} and S_{gr} are irreducible liquid and gas saturations, S_{ls} is a threshold value, P_o is the entry pressure, and λ is a parameter depending on pore geometry.

The relative permeability and capillary pressure curves are illustrated in **Figure S1**. Conventional capillary pressure relationships are applied to model on the macroscale. However, these models have limitations in accurately describing capillary pressure at saturations below the irreducible water saturation, where dry-out and salt precipitation happen. This limitation introduces uncertainty, which will be addressed through alternative capillary pressure curves and sensitivity studies.

Parameters	Values
Irriducible liquid saturation (S_{lr}) [-]	0.3
Critical saturation (S_{ls}) [-]	1
Residual gas saturation (S_{gr})	0.05
Exponent coefficient (m, λ)	0.457
Capillary entry pressure (P_{cr}) [Pa]	19608
Maximum capillary pressure cut-off (P_{max}) [Pa]	1 x 10^7
Fractional length of the pore bodies (Γ) [-]	0.8
Fraction of original porosity (ϕ_r) [-]	0.1 and 0.8

Table S1: List of values that are used to describe capillary pressure, relative permeabilities, and permeability reduction as a function of porosity reduction

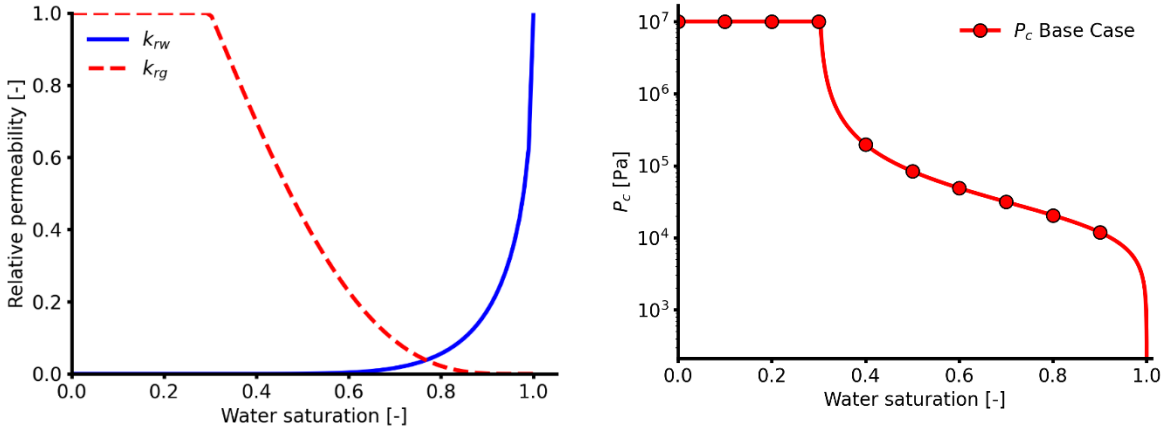

Figure S1: (a) Water and gas relative permeabilities utilized in this study and (b) capillary pressure used for the base case

Salt precipitation in TOUGH2 is modeled by considering the solubility limit of NaCl as a function of temperature, with precipitated salt treated as a solid phase that reduces the porosity. Experimental studies have been shown that small changes in porosity can significantly affect permeability and various models have been proposed to describe this relationship [3–5]. TOUGH2 offers three analytical options for describing permeability as a function of porosity reduction. This study uses the tubes-in-series model [6], which accounts for the converging-diverging nature of porous media.

The model involves two parameters: Γ (fractional length of the pore bodies with two different radii) and ϕ_r (fraction of original porosity define as $\frac{\phi}{\phi_0}$). Equation 6 to Equation 8 describe the tube-in-series model. The parameters used here are Γ = 0.8 and ϕ_r = 0.8, indicating that when 20% of porosity is lost, permeability approaches zero. These values are the standard for most scenarios used in this study, but in sensitivity studies where salt precipitation is uncertain, ϕ_r = 0.1 is used to avoid early reservoir blockage. Corresponding curves are illustrated in **Figure S2**. This correlation, which is a key uncertainty in this study, can significantly impact the injectivity assessment.

$$\frac{k}{k_0} = \theta^2 \left[\frac{1 - \Gamma + \Gamma\, \omega^{-2}}{1 - \Gamma + \Gamma \left(\frac{\theta}{\theta + \omega - 1} \right)^2} \right] \quad \text{Equation 6}$$

$$\theta = \frac{1 - S_s - \phi_r}{1 - \phi_r} \quad \text{Equation 7}$$

$$\omega = 1 + \Gamma^{-1} / (\phi_r^{-1} - 1), \quad \text{Equation 8}$$

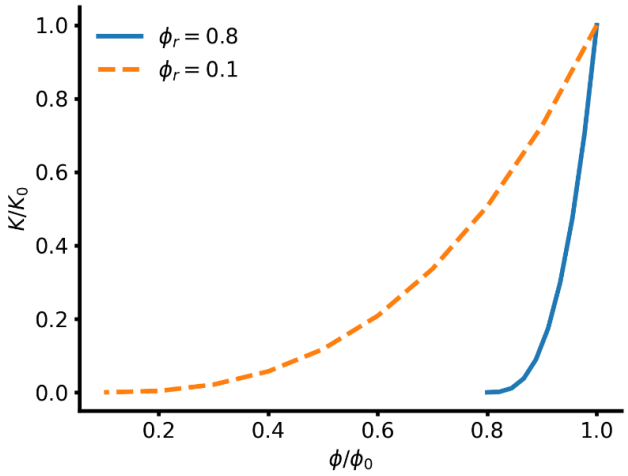

Figure S2: Correlation between porosity and permeability

Description of Cases

Case Name	K [mD]	Rate [kg/s]	P_{cr} [kPa]	S_{lr}	λ	g [m/s^2]
Base case	150	11	20	0.3	0.457	10
Effect of capillary-saturation model choice						
1A_Pc-Log	150	11	20	0	0.3	10
1B_Pc-Slr-neg	150	11	20	0	0.457	10
1C_NoPc	150	11	***	***	***	10
1D_NoPc_No-Kred *	150	11	***	***	***	10
Capillary number (Ca) test cases						
Ca1_0.1R	150	1.1	20	0.3	0.457	10
Ca2_0.01R	150	0.11	20	0.3	0.457	10
Ca3_0.1K	15	11	20	0.3	0.457	10
Ca4_10K	1500	11	20	0.3	0.457	10
Ca5_0.1R_0.1K	15	1.1	20	0.3	0.457	10
Ca6_0.1R_10K	1500	1.1	20	0.3	0.457	10
Ca7_0.01R_0.1K	15	0.11	20	0.3	0.457	10
Ca8_0.01R_10K	1500	0.11	20	0.3	0.457	10
Gravity number (Gr) test cases						
Ca1_0.1R_Gr1	150	1.1	0.2	0.3	0.457	10
Ca1_0.1R_Gr2	150	1.1	0.002	0.3	0.457	10
Ca1_0.1R_Gr3	150	1.1	20	0.3	0.457	1
Ca1_0.1R_Gr4	150	1.1	0.2	0.3	0.457	1

* In addition to neglecting capillary pressure effect, the effect of salt precipitation on permeability reduction is also neglected

*** Capillary pressure has been neglected so the parameters related to the capillary pressure curves are omitted.

Ca1_0.1R_Gr5	150	1.1	0.002	0.3	0.457	1
Ca1_0.1R_Gr6	150	1.1	20	0.3	0.457	0
Ca1_0.1R_Gr7	150	1.1	0.2	0.3	0.457	0
Ca1_0.1R_Gr8	150	1.1	0.002	0.3	0.457	0

Table S2: Description of all cases used in this study.

Effect of Capillary pressure function on salt precipitation

As previously mentioned, conventional capillary pressure curves are inadequate for accurately representing capillary pressure values at water saturations below the irreducible level, which is critical for modeling the dry-out region. To address this limitation, two alternative capillary pressure models are considered in addition to the conventional curve. These are illustrated in **Figure S3**.

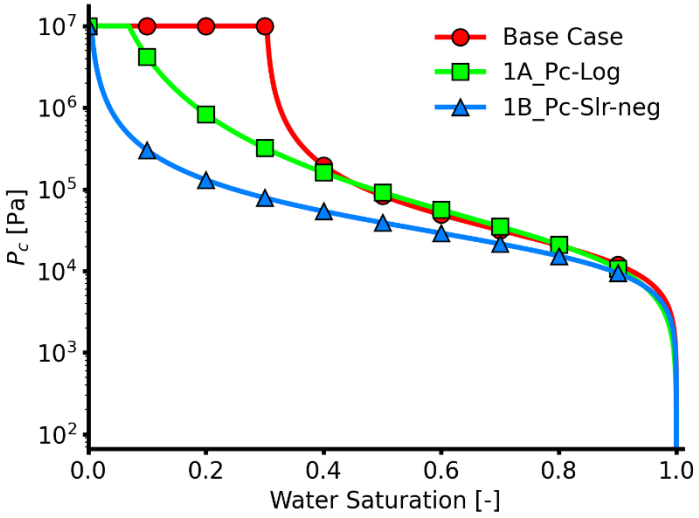

Figure S3: Capillary pressure curves utilized in the Capillary force analysis

The effect of changing the capillary pressure model on salt precipitation profiles is illustrated in **Figure S4**.

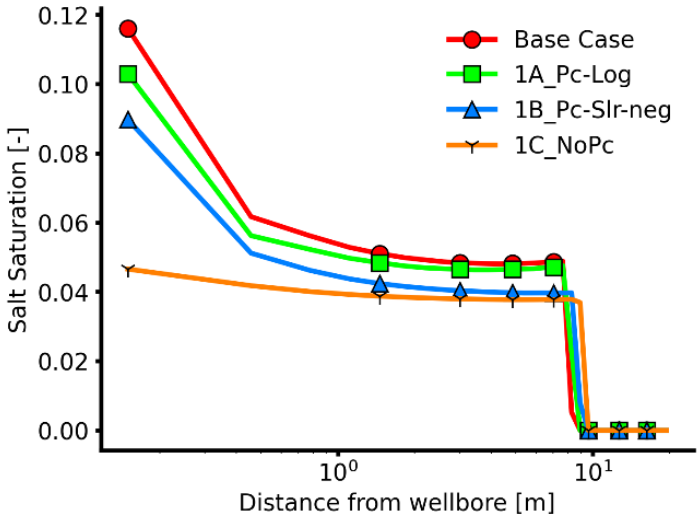

Figure S4: Effect of different capillary functions on salt saturation profile along the bottom line of the reservoir

Effect of Bond Number (Bo)

Investigating scenarios that isolate the influences of gravity and capillary forces while keeping the viscous force constant can provide valuable insights. In several case studies, although the Bo numbers are constant, significant variations in salt precipitation patterns and amounts are observed. This section focuses on the effect of the Bo number on salt precipitation, particularly using the base case with reduced injection rate (Ca1_0.1R), where modifications to capillary entry pressure and gravitational acceleration are implemented. This specific case is chosen due to the presence of a peak in salt precipitation away from the wellbore.

Figure S5 reveals a discernible pattern within each column and row: in each column, the Ca number remains constant while the Bo number increases from top to bottom. Conversely, the Bo number remains constant across each row, while the Ca number decreases from left to right. Throughout these variations, the viscous force remains unchanged due to consistent velocities. Figure S6 illustrates a consistent decline in salt precipitation near the wellbore and a secondary peak further away as the Ca number increases (with Bo held constant). This trend aligns with the relationship concerning backflow, indicating that higher Ca numbers result in decreased salt precipitation near the wellbore.

As the Bo number decreases (indicating stronger gravitational effects), salt precipitation near the wellbore remains largely unchanged, while the secondary peak away from the wellbore diminishes. This suggests that gravity primarily influences salt deposition farther from the injection point. The Ca number strongly affects salt precipitation at the inlet, but no consistent trend is observed for its impact on localized salt deposition. Similarly, the effect of the Bo number on localized precipitation remains inconclusive. Notably, despite constant Bo numbers, localized salt precipitation occurs in multiple cases, whereas reducing the Bo number while maintaining a constant Ca number leads to diminished localized precipitation. These findings indicate that Ca and Bo alone are insufficient to fully describe localized salt precipitation dynamics.

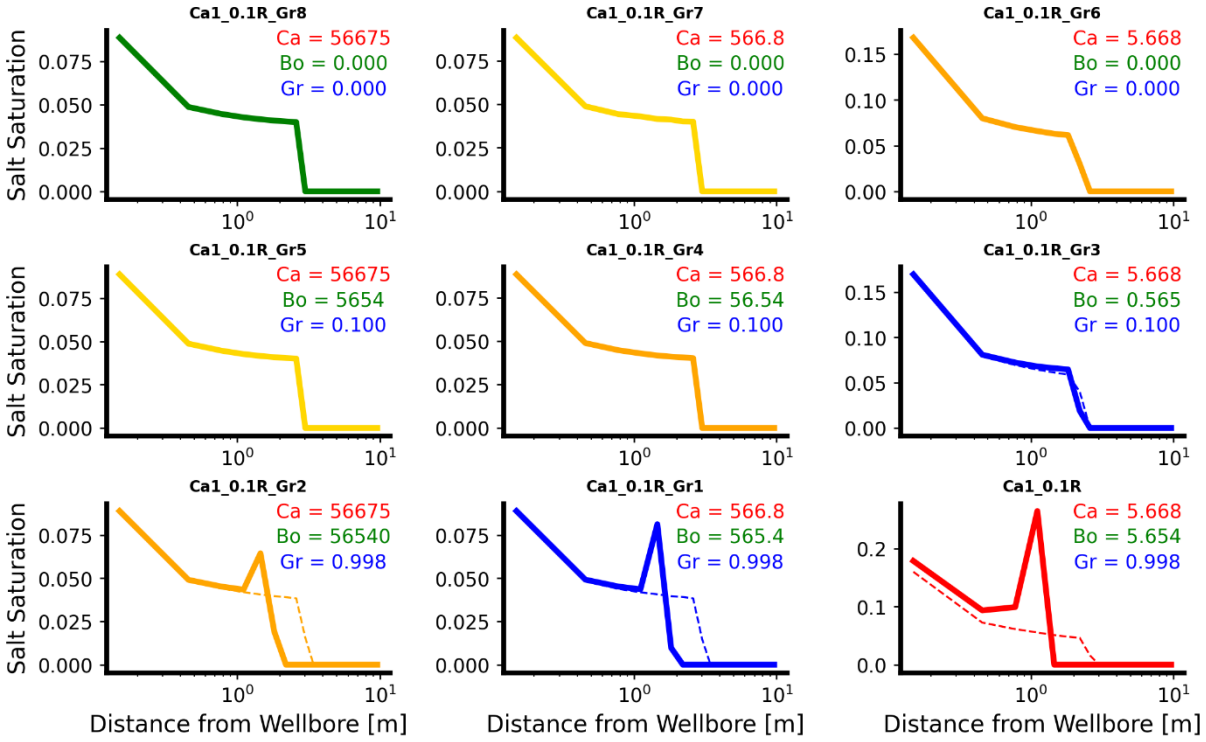

Figure S5: Salt saturation profile as function of Bo numbers. Solid thick and dashed thin lines are profiles along the bottom and top of the reservoir, respectively. Note that in some cases, the bottom and top profiles are indistinguishable.

Effect of capillary pressure and salt precipitation on injection pressure

Increasing capillary pressure increases injection pressure, thus decreasing injectivity through two mechanisms: (a) it raises the pressure needed to penetrate the porous media, and (b) it enhances salt precipitation near the wellbore, which reduces permeability. We recall that the degree of permeability reduction due to salt precipitation is governed by the parameters in Equation 6, which defines the relationship between porosity reduction and permeability.

In **Figure S6**, injection pressure over one year is depicted for three scenarios to illustrate the effects of capillary pressure and salt precipitation on injectivity, maintaining all parameters consistent with the base case. In Case1_NoPC_No-Kred, the influences of capillary pressure and salt precipitation on permeability reduction are disregarded. Case1_NoPC excludes only capillary pressure. The comparison between Case1_NoPC and Case1_NoPC_No-Kred highlights the effects of permeability reduction due to salt precipitation. Conversely, the difference between Case1 and Case1_NoPC illustrates the combined effects of capillary pressure and permeability reduction from salt precipitation, showing a greater pressure difference than in the previous comparison. This indicates that injectivity loss is most sensitive to capillary pressure effects in this case.

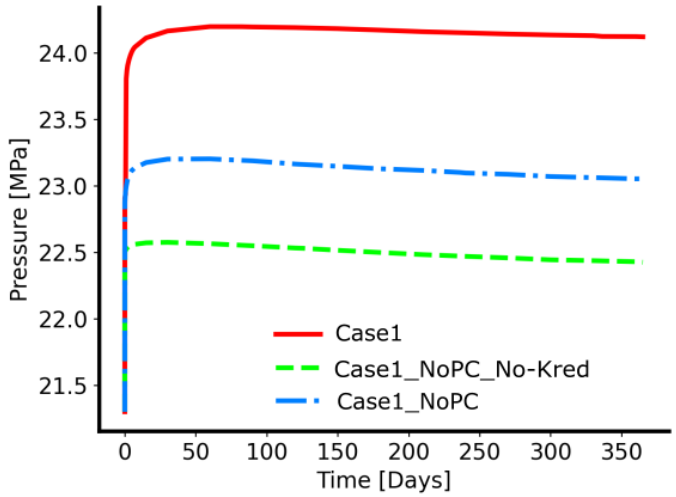

Figure S6: Effect of capillary pressure and salt precipitation on injection pressure

Data Extracted from Literature

Parameters extracted from Kim et al. (2012) and all cases used for the calculation of Ca, Bo, and Gr numbers are summarized in **Table S3**.

Case Name	Rate [kg/s]	Permeability [mD]	Vcr [m/s]	Ca	Bo	Gr	Localized Salt-precip.
Case1_kim	1	10	1.26514e−4	3,07E+02	8,33E+01	2,71E-01	No

Case1-1_Kim	2	10	2.53029e-4	6,14E+02	8,33E+01	1,36E-01	No
Case1-2_kim	3	10	3.79543e-4	9,22E+02	8,33E+01	9,04E-02	No
Case1-3_kim	4	10	5.06057e-4	1,23E+03	8,33E+01	6,78E-02	No
Case1-4_kim	5	10	6.32571e-4	1,54E+03	8,33E+01	5,42E-02	No
Case2_kim	2,5	50	3.16286e-4	1,54E+02	8,33E+01	5,42E-01	**Yes**
Case2-1_Kim	5	50	6.32571e-4	3,07E+02	8,33E+01	2,71E-01	**Yes**
Case2-2_kim	10	50	1.26514e-3	6,14E+02	8,33E+01	1,36E-01	No
Case2-3_kim	20	50	2.53029e-3	1,23E+03	8,33E+01	6,78E-02	No
Case2-4_kim	30	50	3.79543e-3	1,84E+03	8,33E+01	4,52E-02	No
Case3_Kim	3	100	3.79543e-4	9,22E+01	8,33E+01	9,04E-01	**Yes**
Case3_1_Kim	5	100	6.32571e-4	1,54E+02	8,33E+01	5,42E-01	**Yes**
Case3-2_Kim	10	100	1.26514e-3	3,07E+02	8,33E+01	2,71E-01	**Yes**
Case3-3_Kim	20	100	2.53029e-3	6,14E+02	8,33E+01	1,36E-01	No
Case3-4_Kim	30	100	3.79543e-3	9,22E+02	8,33E+01	9,04E-02	No
Base Case	11	150	2.68e-3	57	0.1	5.7	No
Ca1_0.1R	1.1	150	2.68e-4	5.7	1	5.7	**Yes**
Ca2_0.01R	0.11	150	2.68e-5	0.57	0.01	5.7	NO
Ca3_0.1K	11	15	2.68e-3	570	0.01	5.7	NO
Ca4_10K	11	1500	2.68e-3	5.7	1	5.7	**Yes**
Ca5_0.1R_0.1K	1.1	15	2.68e-4	57	0.1	5.7	No
Ca6_0.1R_10K	1.1	1500	2.68e-4	5.7	1	5.7	No
Ca7_0.01R_0.1K	0.11	15	2.68e-5	0.57	10	5.7	**Yes**
Ca8_0.01R_10K	0.11	1500	2.68e-5	0.06	100	5.7	No
Ca1_0.1R_Gr1	1.1	150	2.68e-4	570	1	570	**Yes**
Ca1_0.1R_Gr2	1.1	150	2.68e-4	56700	1	56700	**Yes**
Ca1_0.1R_Gr3	1.1	150	2.68e-4	5.7	0.1	0.57	No
Ca1_0.1R_Gr4	1.1	150	2.68e-4	567	0.1	56.7	No
Ca1_0.1R_Gr5	1.1	150	2.68e-4	56700	0.1	5670	No
Ca1_0.1R_Gr6	1.1	150	2.68e-4	5.7	0	0	No
Ca1_0.1R_Gr7	1.1	150	2.68e-4	570	0	0	No
Ca1_0.1R_Gr8	1.1	150	2.68e-4	56700	0	0	No

Table S3: Summary of parameter values extracted from Kim et al. (2012). The width of reservoir is 100 m. Pcr is 1.96e3 [Pa], g is 10 m/s^2, porosity is 0.2, viscosity is 4.76e-5 Pa.s and density is 629 kg/m^3.

Effect of Heterogeneity

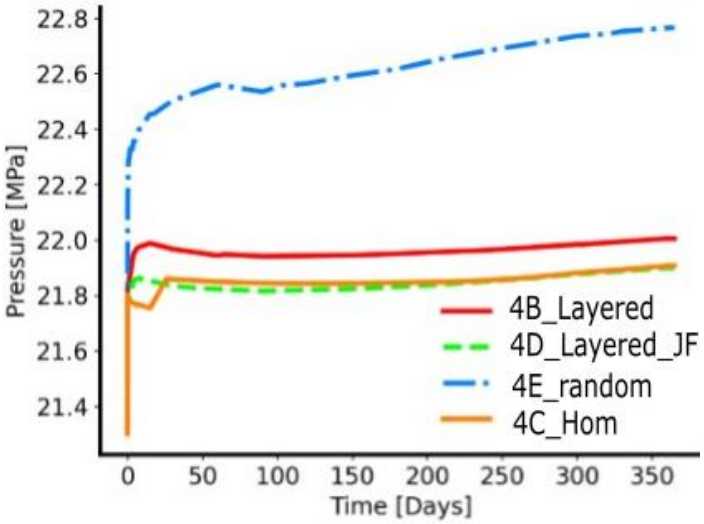

Figure S7: Comparison of injection pressure for different heterogeneous scenarios and one homogeneous case

Data Availability

The TOUGH2 input files used to generate the results presented in this paper can be found at https://github.com/cssr-tools/saltprectough2.

References

(1) Pruess, K. The TOUGH Codes—A Family of Simulation Tools for Multiphase Flow and Transport Processes in Permeable Media. *Vadose Zone Journal* **2004**, *3* (3), 738–746. https://doi.org/10.2136/VZJ2004.0738.

(2) Pruess, K.; Spycher, N. ECO2N – A Fluid Property Module for the TOUGH2 Code for Studies of CO2 Storage in Saline Aquifers. *Energy Convers Manag* **2007**, *48* (6), 1761–1767. https://doi.org/10.1016/J.ENCONMAN.2007.01.016.

(3) Zhang, D.; Kang, Y.; Selvadurai, A. P. S.; You, L. Experimental Investigation of the Effect of Salt Precipitation on the Physical and Mechanical Properties of a Tight Sandstone. *Rock Mech Rock Eng* **2020**, *53* (10), 4367–4380. https://doi.org/10.1007/S00603-019-02032-Y/FIGURES/11.

(4) Miri, R.; Hellevang, H. Salt Precipitation during CO 2 Storage-A Review. *International Journal of Greenhouse Gas Control* **2016**, *51*, 136–147. https://doi.org/10.1016/j.ijggc.2016.05.015.

(5) Le, D.; Mahadevan, J. Productivity Loss in Gas Wells Caused by Salt Deposition. *SPE Journal* **2011**, *16* (04), 908–920. https://doi.org/10.2118/132606-PA.

(6) Verma, A.; Pruess, K. Thermohydrological Conditions and Silica Redistribution near High-Level Nuclear Wastes Emplaced in Saturated Geological Formations. *J*

Geophys Res Solid Earth **1988**, *93* (B2), 1159–1173. https://doi.org/10.1029/JB093IB02P01159.

(7) Kim, K. Y.; Han, W. S.; Oh, J.; Kim, T.; Kim, J. C. Characteristics of Salt-Precipitation and the Associated Pressure Build-Up during CO 2 Storage in Saline Aquifers. *Transp Porous Media* **2012**, *92* (2), 397–418. https://doi.org/10.1007/S11242-011-9909-4/METRICS.

(8) Pruess, K.; Müller, N. Formation Dry-out from Co2 Injection into Saline Aquifers: 1. Effects of Solids Precipitation and Their Mitigation. *Water Resour Res* **2009**, *45* (3). https://doi.org/10.1029/2008WR007101.